

Unified Electronic Phase Diagram for Hole-Doped High- T_c Cuprates

T. Honma

Department of Physics,
Asahikawa Medical College, Asahikawa, Hokkaido 078-8510, Japan*

P. H. Hor

Department of Physics and Texas Center for Superconductivity,
University of Houston, Houston, TX. 77204-5005, USA⁺

We have analyzed various characteristic temperatures and energies of hole-doped high- T_c cuprates as a function of a dimensionless hole-doping concentration (p_u). Entirely based on the experimental grounds we construct a unified electronic phase diagram (UEPD) where three characteristic temperatures (T^* s) and their corresponding energies (E^* s) converge as p_u increases in the underdoped regime. T^* s and E^* s merge together with the T_c curve and $3.5k_B T_c$ curve at $p_u \sim 1.1$ in the overdoped regime, respectively. They finally go to zero at $p_u \sim 1.3$. The UEPD follows an asymmetric half-bell-shaped T_c -curve in which T_c appears at $p_u \sim 0.4$, reaches a maximum at $p_u \sim 1$, and rapidly goes to zero at $p_u \sim 1.3$. The asymmetric half-bell-shaped T_c -curve is at odds with the well-known symmetric superconducting dome for $\text{La}_{2-x}\text{Sr}_x\text{CuO}_4$ (SrD-La214) in which two characteristic temperatures and energies converge as p_u increases and merge together at $p_u \sim 1.6$, where T_c goes to zero. The UEPD clearly shows that pseudogap phase precedes and coexists with high temperature superconductivity in the underdoped and overdoped regimes, respectively. It is also clearly seen that the upper limit of high- T_c cuprate physics ends at a hole concentration that equals to 1.3 times the optimal doping concentration for almost all high- T_c cuprate materials, and 1.6 times the optimal doping concentration for the the SrD-La214. Our analysis strongly suggests that pseudogap is necessary for high temperature superconductivity and the normal state of both underdoped and overdoped regimes can not be regarded as a conventional Fermi liquid phase.

PACS; 74.25.Fy, 74.72.-h, 74.25.Dw

I. Introduction

The unique hallmark of high temperature superconductors (HTS's) is a pseudogap phase characterized by the observation of a multiple pseudogap temperatures (T^* 's) and pseudogap energies (E^* 's) by a large number of different experimental probes. While the pseudogap phase precedes the high temperature superconducting phase characterized by the superconducting transition temperature (T_c) and superconducting gap energy (Δ_c), it is not clear how the T^* , T_c , E^* and Δ_c are related to each other. Specifically, how are T^* and E^* related to the occurrence of the high- T_c superconductivity is still unclear. Is pseudogap a sufficient and/or necessary condition for high- T_c or is it just a complication of specific material systems? Is it collaborating or competing with superconductivity? For instance, it is argued that the pseudogap is a competing order that may have nothing to do with high- T_c .¹ On the other hand it is also suggested that the pseudogap is intimately related with high- T_c .^{2,3} To distinguish these two contradictory pictures that are critical to the mechanism of high- T_c superconductivity requires a comparison of various characteristic temperatures and energies in a universal phase diagram for all HTS's. Any systematic behavior derived from this kind of phase diagram will provide true intrinsic properties of HTS that are free from material-specific complications. However, until now there is no such a comparison made and no such phase diagram available. In this paper we present a unified electronic phase diagram for almost all HTS's.

In the single-layer $\text{La}_{2-x}\text{Sr}_x\text{CuO}_4$ (SrD-La214), where the hole-doping concentration can be unambiguously determined from the Sr-content (x),⁴ the $T_c(x)$ exhibits a well-known symmetric bell-shaped curve, the so-called superconducting dome, with a maximum T_c (T_c^{max}) locating at $x \sim 0.16$.⁵ Assuming that all HTS materials have the identical symmetric superconducting dome, this relation was reduced to the following formula

$$1 - T_c/T_c^{max} = 82.6(P_{T_c} - 0.16)^2. \quad (1)$$

Equation (1) has been widely used to determine the hole-doping concentration (P_{T_c}) for many other HTS's.^{5,6,18,44,62,71,72,75,77,80,82,86,90,96,99-103} Using this hole-scale based on the superconducting dome, the P_{T_c} -scale, various phase diagrams have been constructed.¹ A distinct feature in one of such phase diagrams is that T^* crosses the superconducting

dome and reaches zero at a quantum critical point (QCP) inside the dome.^{1,6} On the other hand, without using the P_{T_c} -scale, some qualitative experimental observations seem to support another picture where T^* touches the superconducting dome at around T_c^{max} and merges into the superconducting dome without QCP.² To distinguish these two fundamentally different pictures we need a hole-scale that can reveal the true intrinsic doping dependences of T^* , T_c , E^* and Δ_c .

The common structural features of HTS are CuO_2 -planes that host the doped holes and the block layers that supply the holes into the planes through oxygen-doping and/or cation-doping. While the doped hole-carriers are initially confined in the CuO_2 -planes sandwiched between the insulator-like block layers, the holes are partially deconfined from the planes with doping. Therefore, the lightly doped HTS generally shows strongly two-dimensional (2D) properties. But, as the hole-doping increases, some physical properties are 2D and some, although built on the 2D carriers, will nominally be three-dimensional (3D) in nature. Therefore, it is necessary to use 2D and 3D carrier-doping concentrations to address 2D and 3D physical properties, respectively. To quantitatively study such dimensionality-dependent physical properties we have proposed a universal **planar** hole-scale (P_{pl} -scale) for determining the hole-doping content per CuO_2 plane (P_{pl}).⁷ In this scale, the P_{pl} is uniquely determined from the thermoelectric power (TEP) at 290 K (S^{290}).⁷ We showed that, in Ref. 7, the P_{pl} -scale is independent of the nature of the dopant, the number of CuO_2 -plane layers per unit cell (n_{layer}), the structure and the sample quality, namely, single crystal or not. This universal $S^{290}(P_{pl})$ -relationship is built on the sound experimental observations although it, similar to the situation of the most popular P_{T_c} -scale, is still mainly empirical and waited to be justified theoretically. Since the average area per copper in CuO_2 -plane is almost independent of the HTS materials, therefore the P_{pl} is essentially equal to 2D hole-doping concentration defined as the hole-doping content per unit area. Using the 2D P_{pl} -scale, it was found in the phase diagram for all major HTS's plotted as a function of P_{pl} that the T^* -curves are independent of the layer number per formula unit cell while the T_c -curve strongly depends on it.⁷ Therefore the P_{pl} -scale is intrinsically consistent with the pseudogap energy scale.⁷ We can also define an effective 3D hole-doping concentration (P_{3D}) by a simple conversion formula $P_{3D} \equiv P_{pl} \times (n_{layer}/V_{u.c.})$, where $V_{u.c.}$ is the unit cell volume.⁸ Since the P_{3D} is essentially

the hole-doping content per unit volume, therefore, this natural extension of P_{pl} -scale to P_{3D} (P_{3D} -scale) has allowed us to address the corresponding 3D properties.⁸ For instance, in the case of the single-layer HTS, the Hall number per “ cm^3 ”, calculated from the Hall coefficient, is not scaled with P_{pl} but P_{3D} .⁸ The $\tau_c(T_c)$, a reduced temperature-scale defined as $\tau_c(T) \equiv T/T_c^{max}$, of the single-layer HTS universally appears at $6 \times 10^{20} \text{ cm}^{-3}$ and reaches a universal maximum value at $1.6 \times 10^{21} \text{ cm}^{-3}$ as shown in Fig. 1(b),⁸ although their critical hole-doping concentrations on the P_{pl} -scale depend on the materials as shown in Fig. 1(a).⁷ Thus, it was shown that various normal and superconducting properties for many different material systems can be compared consistently by using either P_{pl} or P_{3D} .⁷⁻⁹

In order to reveal the intrinsic generic electronic properties of all HTS's, it is necessary to be able to put both 2D and 3D physical properties on a single phase diagram. To achieve this goal, we need a carrier-scale that is not only independent of the material system but also independent of the dimensionality of the physical properties. This can be achieved if, for each material system, we scale the P_{pl} and P_{3D} with their corresponding optimal doping concentrations, P_{pl}^{opt} and P_{3D}^{opt} , respectively. Here, we introduce a dimensionless unified hole-doping concentration, p_u ($p_u \equiv P_{pl}/P_{pl}^{opt} = P_{3D}/P_{3D}^{opt}$). This unified hole-scale (p_u -scale) can be used for all physical properties, independent of their dimensionality, in all HTS's. Indeed, the identical doping dependent behaviors are preserved when $\tau_c(T_c)$ of the single-layer HTS plotted as a function of P_{3D} in Fig. 1(b) was replotted as a function of p_u in Fig. 1(c).¹⁰⁻²⁰ Here, the $(P_{pl}^{opt}, T_c^{max})$ of the HgBa₂CuO_y (OD-Hg1201)^{14,15} and Bi₂Sr_{2-x}La_xCuO_{6+δ} (CD-Bi2201)¹⁶ are determined to be (0.235,97) and (0.28,35.5) from the Fig. 1(a), respectively. For the other materials, each P_{pl}^{opt} is determined from the plot of T_c vs P_{pl} for the each compound in the present work or Refs. 7-9. For the Tl₂Ba₂CuO_{6+δ} (OD-Tl2201) there is few report on the optimally doped samples because the optimally doped OD-Tl2201 is hard to prepare. In this case we use the highest $T_c = 93 \text{ K}$ among the published data as T_c^{max} .²¹ From the plot of T_c vs P_{pl} in Fig. 1(a), the optimal P_{pl} is estimated to be ~ 0.25 . Essentially we can view p_u as a scaled dimensionality- and material- independent universal carrier-doping concentration that preserves the intrinsic doping dependency for **any** physical property for **all** HTS's. In this report, we analyze almost all characteristic temperatures and

energies as a function of p_u . We find a dopant-specific unified electronic phase diagram for HTS. The dominate phase diagram is an asymmetric half-bell-shaped T_c -curve for the cation and anion (oxygen) co-doped (CD) HTS. The T_c for the purely oxygen-doped (OD) HTS also follows the half-bell-shaped T_c -curve with some indication of the influence of the thermally induced oxygen redistribution. Only the SrD-La214 which is the purely cation-doped HTS follows the well-known superconducting dome or symmetric bell-shaped T_c -curve.

II. Analysis

The details of how the P_{pl} - and P_{3D} -scales were constructed had been reported in Refs. 7 and 8 respectively. In this paper, we analyzed many published data by the p_u -scale. The determination of P_{pl} based on the TEP is most reliable. Accordingly, the data including TEP are selected among the accumulated published data. The second reliable determination of P_{pl} is determined from the value of T_c using T_c vs P_{pl} curve for each compound reported in Refs. 7-9. When the data with P_{Tc} is analyzed, the P_{Tc} is converted into P_{pl} by using the relation in Fig 2(c) discussed below. To clearly label the origin of P_{pl} or p_u for each sample or data set plotted in Figs. 3 – 6, we use the following superscripted character to designate: *a.* P_{pl} is determined by T_c vs P_{pl} curve for the each compound in Refs. 7-9 if the cited data have no TEP but T_c ; and *b.* P_{pl} is converted from P_{Tc} by using the relation in Fig. 2(c) if the cited data has P_{Tc} . For instance, OD-Hg1201^a, *name*^a or Refs. X-Y^a indicate that sample OD-Hg1201, the data identified by author *name et al.*, the data contained in Refs. X-Y for a particular sample has no TEP but T_c and therefore the P_{pl} is determined by T_c vs P_{pl} curve reported in Refs. 7-9, respectively. Whenever there is no superscripted character, the P_{pl} is determined directly from the TEP.

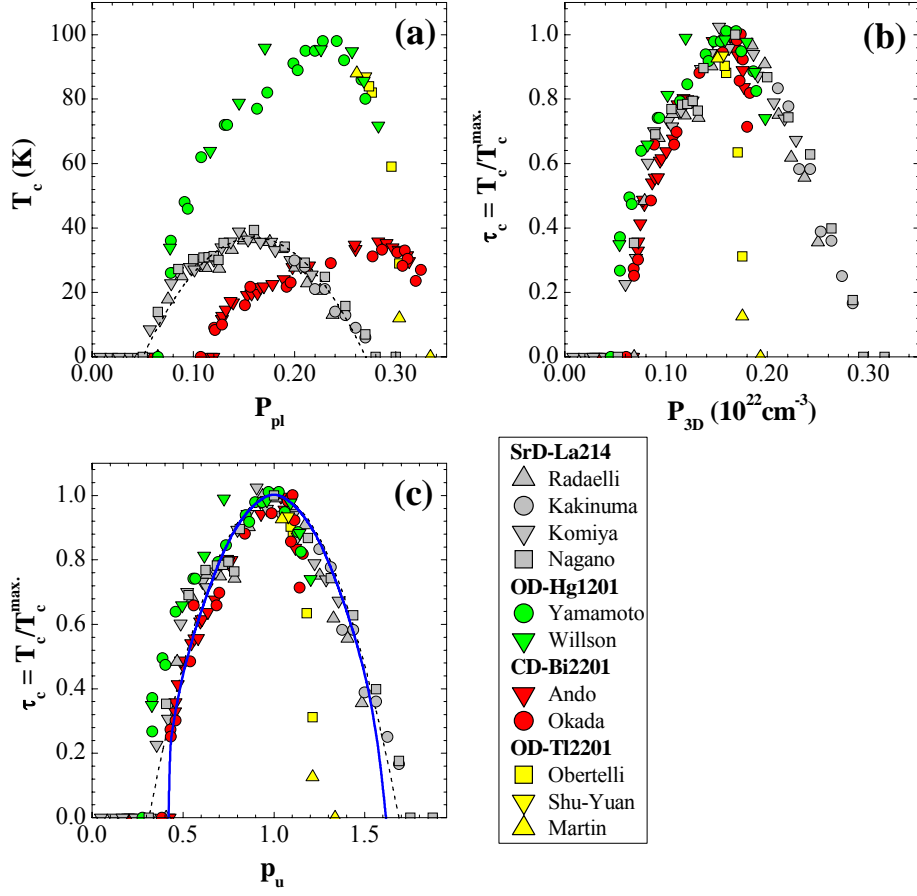


FIG. 1. (a) The superconducting transition temperature (T_c) of the single-layer HTS as a function of P_{pl} . The reduced superconducting transition temperature $\tau_c(T_c) (\equiv T_c/T_c^{max})$ of the single-layer HTS as a function of (b) the effective 3D hole-doping concentration P_{3D} , and (c) the unified hole-doping concentration p_u . The plotted data were cited from Refs. 10-13 for $\text{La}_{2-x}\text{Sr}_x\text{CuO}_4$ (SrD-La214), Refs. 14 and 15 for $\text{HgBa}_2\text{CuO}_{4+\delta}$ (OD-Hg1201), Refs. 16 and 17 for $\text{Bi}_2\text{Sr}_{2-x}\text{La}_x\text{CuO}_{6+\delta}$ (CD-Bi2201) and Refs. 18-20 for $\text{Tl}_2\text{Ba}_2\text{CuO}_{6+\delta}$ (OD-Tl2201). The broken line comes from the equation (1). The solid line is the superconducting dome.

III. Results and Discussion

A. Universal Hole-Doping Scale

First of all, we demonstrate how the hole-doping scale based on the S^{290} is effective and universal. In Figs. 2(a) and 2(b), we plot the S^{290} of sintered sample and in-plane S^{290} of the single crystal as a function of P_{pl} , together with previously reported data.⁷ S^{290} (≥ 7 $\mu\text{V/K}$) on the upper panel is plotted on a logarithmic scale, while S^{290} (< 7 $\mu\text{V/K}$) on the lower panel is plotted on a linear scale. The plotted data are coming from $\text{Y}_{1-x}\text{Ca}_x\text{Ba}_2\text{Cu}_3\text{O}_6$ (CaD-Y1236),⁷ SrD-La214 ,^{13,22-28} $\text{La}_{2-x}\text{Ba}_x\text{CuO}_4$ (BaD-La214),²⁹ $\text{La}_2\text{CuO}_{4+\delta}$ (OD-La214),³⁰ CD-Bi2201 ,^{31,32} $(\text{Nd}_{1.6-x}\text{Ce}_x\text{Sr}_{0.4})\text{CuO}_4$ (CeD-NdSr214)³³ and $(\text{La}_{1.6-x}\text{Nd}_{0.4}\text{Sr}_x)\text{CuO}_4$ (SrD-LaNd214)³⁴ as the single-layer HTS, $\text{HgBa}_2\text{CaCu}_2\text{O}_{6+\delta}$ (OD-Hg1212),³⁵ $(\text{Hg}_{0.5}\text{Fe}_{0.5})\text{Sr}_2(\text{Y}_{1-x}\text{Ca}_x)\text{Cu}_2\text{O}_y$ (CD-Hg1212)³⁶ as the double-layer HTS, and underdoped $\text{HgBa}_2\text{Ca}_2\text{Cu}_3\text{O}_{8+\delta}$ (OD-Hg1223)³⁵ as the triple-layer HTS. The P_{pl} of SrD-La214 without excess oxygen is equal to Sr-content.⁴ The P_{pl} of CaD-Y1236, which the oxygen-content was determined to be 6 by the iodometric titration in Ar gas,⁷ can be unambiguously and directly determined as a half of the Ca-content, since the CaD-Y1236 has the isolated Cu layer in stead of CuO chain. In fact, it is shown by the O 1s and Cu 2p near edge x-ray absorption fine structure (NEXAFS) experiment that the holes introduced by replacing Y^{3+} with Ca^{2+} appear solely in the CuO_2 planes without affecting the isolated Cu layer in the CaD-Y1236.⁴⁰ The P_{pl} for the other materials were determined from the copper valancy measured by the iodometric titration for the OD-La214³⁰ and CD-Bi2201,^{31,32} and the double iodometric titration for the OD-Hg1212,³⁵ CD-Hg1212³⁶ and OD-Hg1223.³⁵ Noticed that the plotted data follow the universal $S^{290}(P_{pl})$ -curve proposed in Ref. 7, irrespective of the nature of dopant, n_{layer} , the structure and the sample quality, namely, single crystal or not. It is also independent from whether the CuO_2 plane is surrounded by the octahedral or pyramidal oxygen coordination. For the SrD-La214, there is the upward deviation from the universal line at $P_{pl} > 0.25$. This deviation is considered to be due to the oxygen-deficient that was reported to be significant over $x = P_{pl} \sim 0.25$.¹⁰ In the CeD-NdSr214, the upward deviation over $P_{pl} \sim 0.15$ from the universal line can be explained by the oxygen deficiency generating the

hole deficient of ~ 0.05 as pointed out in Ref. 33. Therefore, the proposed universal $S^{290}(P_{pl})$ -curve that based purely on the experimental grounds works well as the empirical intrinsic hole-scale for the HTS in the range of $0.01 < P_{pl} < 0.34$. In Fig. 2(c), we compare the P_{pl} with P_{Tc} . The solid line shows the P_{pl} as a function of P_{Tc} . The broken line shows $P_{pl} = P_{Tc}$. The quantitative difference between the P_{pl} -scale and the P_{Tc} -scale becomes clear in Fig 2(c). In addition we used this relation for the conversion from P_{Tc} into P_{pl} when the data plotted here have the P_{Tc} without TEP.

Next, we compare our universal scale based on the S^{290} to that determined by other techniques. In Fig 3, we plot the hole-doping concentration determined by the ARPES, nuclear quadrupole resonance (NQR) frequency, NEXAFS and polar angular magnetoresistance oscillations (AMRO) as a function of P_{pl} . The hole-doping concentration by ARPES (P_{ARPES}) is deduced from the area of the experimental Fermi surface (FS) observed in SrD-La214,^{37,38} $(\text{Bi}_{1.74}\text{Pb}_{0.38})\text{Sr}_{1.88}\text{CuO}_{6+\delta}$ (OD-PbBi2201) and $(\text{Bi}_{1.35}\text{Pb}_{0.85})(\text{Sr}_{1.47-x}\text{La}_{0.38+x})\text{CuO}_{6+\delta}$ (CD-PbBi2201).³⁹ The planar hole-doping concentration is also determined by NEXAFS (P_{NEXAFS}) in CaD-Y1236,⁴⁰ $\text{YBa}_2\text{Cu}_3\text{O}_{6+\delta}$ (OD-Y123)^{40a} and $\text{Y}_{0.9}\text{Ca}_{0.1}\text{Ba}_2\text{Cu}_3\text{O}_{6+\delta}$ ^{40a}; by NQR (P_{NQR}) in OD-Y123^{41a} and OD-Tl2201;^{41a} and by AMRO (P_{AMRO}) in OD-Tl2201.^{42a} It can be clearly seen that the P_{pl} determined by TEP is quite consistent with P_{NEXAFS} and P_{NQR} . Although there is a slight scattering, the P_{pl} is also consistent with P_{ARPES}^{FS} and P_{AMRO} . Thus, our P_{pl} -scale is consistent with above other scales. Accordingly, the present p_u -scale is also intrinsically consistent with the hole concentrations determined by the above techniques.

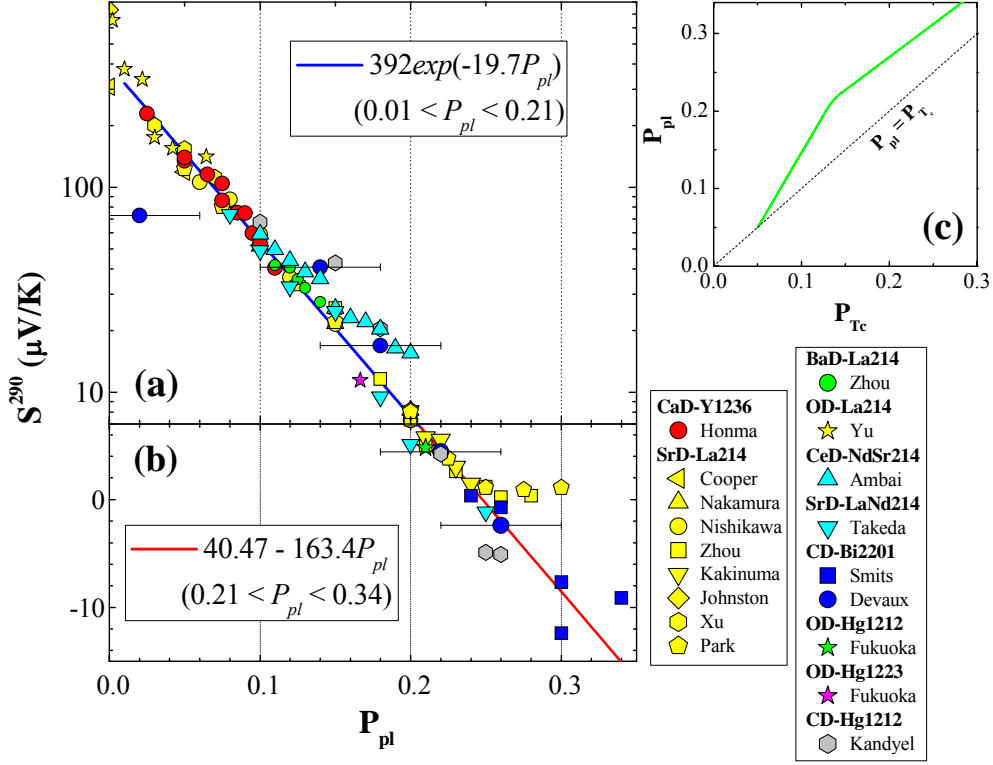


FIG. 2. Room temperature thermoelectric power (S^{290}) as a function of the hole-doping content per CuO_2 plane. (a) S^{290} ($\geq 7 \mu\text{V/K}$) on the upper panel is plotted on a logarithmic scale, while (b) S^{290} ($< 7 \mu\text{V/K}$) on the lower panel is plotted on a linear scale. The plotted data are coming from SrD-La214,^{13,22-28} $\text{La}_{2-x}\text{Ba}_x\text{CuO}_4$ (BaD-La214),²⁹ $\text{La}_2\text{CuO}_{4+\delta}$ (OD-La214),³⁰ CD-Bi2201,^{31,32} $(\text{Nd}_{1.6-x}\text{Ce}_x\text{Sr}_{0.4})\text{CuO}_4$ (CeD-NdSr214)³³ and $(\text{La}_{1.6-x}\text{Nd}_{0.4}\text{Sr}_x)\text{CuO}_4$ (SrD-LaNd214)³⁴ as the single-layer HTSC, CaD-Y1236,⁷ $\text{HgBa}_2\text{CaCu}_2\text{O}_{6+\delta}$ (OD-Hg1212),³⁵ $(\text{Hg}_{0.5}\text{Fe}_{0.5})\text{Sr}_2(\text{Y}_{1-x}\text{Ca}_x)\text{Cu}_2\text{O}_{6+\delta}$ (CD-Hg1212)³⁶ as the double-layer HTS, and underdoped $\text{HgBa}_2\text{Ca}_2\text{Cu}_3\text{O}_{8+\delta}$ (OD-Hg1223)³⁵ as the triple-layer HTS. (c) Quantitative comparison between P_{pl} and P_{Tc} . The solid line shows the P_{pl} as a function of P_{Tc} . The dotted line shows $P_{pl} = P_{Tc}$. We used this relation for the conversion from P_{Tc} into P_{pl} since the data plotted here have the P_{Tc} determined from the S^{290} by using the S^{290} vs P_{Tc} relation in Ref. 18.

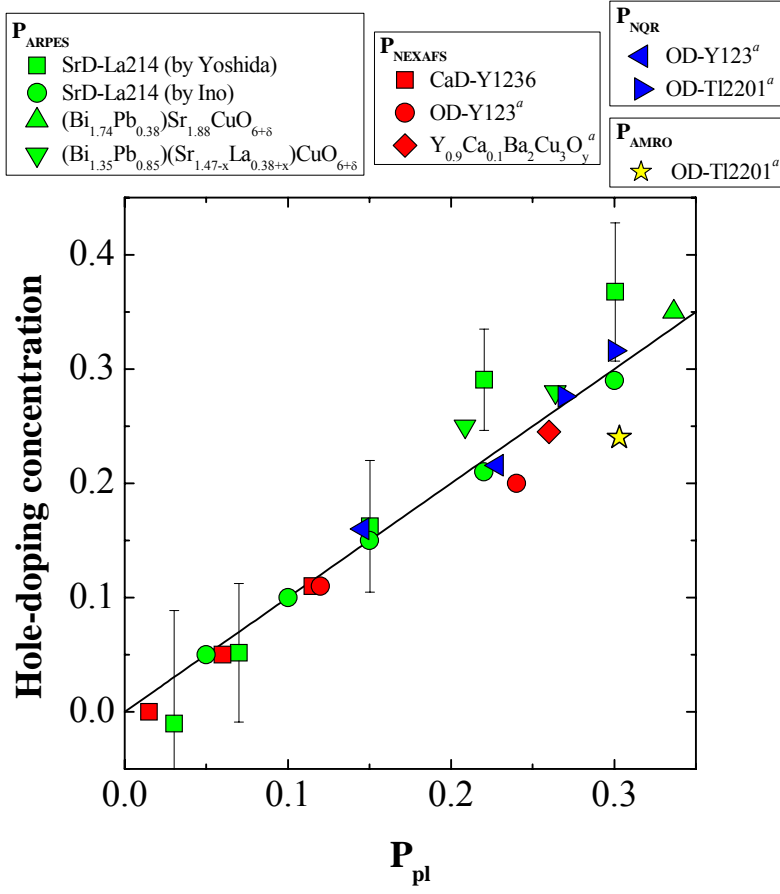


FIG. 3. Hole-doping content per Cu determined by various techniques as a function of P_{pl} . The data for P_{ARPES} , P_{NEXAFS} , P_{NQR} and P_{AMRO} are coming from Refs. 37-39, Ref. 40^a, Ref. 41^a and Ref. 42^a, respectively.

B. Asymmetric Half-bell-shaped T_c -curve

In Fig. 4(a), we plot the T_c and resistive pseudogap temperature (T_ρ^*) of all the $\text{YBa}_2\text{Cu}_3\text{O}_{6+\delta}$ (OD-Y123) related materials which do not have significant contribution of CuO chain as a function of p_u . It includes $\text{Y}_{1-x}\text{Ca}_x\text{Ba}_2\text{Cu}_3\text{O}_{6+\delta}$ (CD-Y123),^{6b,43,44} $(\text{Ca}_{0.4}\text{La}_{0.6})(\text{Ba}_{1.35}\text{La}_{0.65})\text{Cu}_3\text{O}_{7+\delta}$ (CLBLCO),⁴⁵ and $\text{CaLaBaCu}_3\text{O}_{6+\delta}$ (CLBCO).⁴⁶ First we note that the $T_c(p_u)$ does not follow the well-known superconducting dome shown as a dotted line in the Fig. 4(a), instead, it follows an asymmetric half-bell-shaped curve shown as a solid line. Although T_c in the underdoped regime basically follows the superconducting dome, T_c in the overdoped regime decreases much more rapidly. In the same Fig. 4(a) the T_ρ^* , temperature where the high temperature T -linear resistivity bends downward,^{47a} decreases with doping, smoothly merges into the half-bell shaped T_c -curve and finally tends to reach an end point located at $(p_u, T) = (1.3, 0)$. Therefore, in contrast to the proposal that the T_ρ^* -curve crosses the T_c -curve,¹ the $T_\rho^*(p_u)$ -curve smoothly merges into the T_c -curve in the overdoped regime. In Fig. 4(b), we plot the T_c and T_ρ^* as a function of p_u for $\text{Y}_{0.8}\text{Ca}_{0.2}\text{Ba}_2(\text{Cu}_{1-x}\text{Zn}_x)_3\text{O}_{6+\delta}$ for $0 \leq x \leq 0.04$.^{6b} Although the $T_\rho^*(p_u)$ slightly depends on Zn-content in the overdoped regime, the $T_\rho^*(p_u)$ again tends to merge into $T_c(p_u)$ at the overdoped regime. This should be compared to the original plot, based on the P_{T_c} -scale, in which T_ρ^* crossed the superconducting dome and reached zero at a proposed QCP ($P_{T_c} = 0.19$).⁶ Accordingly, the crossing was an artifact that came from two sources; one is the use of a hole-scale that failed to take into account the differences in dimensionality of different physical properties, namely, the two-dimensional T_ρ^* vs three-dimensional T_c , **and** the other is that the T_c -curve for the majority of HTS follows the asymmetric bell-shaped curve, **only** SrD-La214 follows the symmetric bell-shaped T_c -curve or superconducting dome.

The $\tau_c(T_c)$ vs p_u plot for the cation and oxygen co-doped HTS and the purely oxygen-doped HTS are shown in Figs. 5(a) and (b), respectively. We designate all co-doped samples such as CD-Y123,^{6b,43,44,48} CLBLCO,⁴⁵ CLBCO,⁴⁶ $\text{Bi}_2\text{Sr}_2\text{Ca}_{1-x}\text{Y}_x\text{Cu}_2\text{O}_{8+\delta}$ (CD-Bi2212),^{50,51} CD-Bi2201,^{16,17} $\text{Tl}_{1-x}\text{Pb}_x\text{Sr}_2\text{Ca}_{1-y}\text{Y}_y\text{Cu}_2\text{O}_{6+\delta}$ (CD-TlPb1212),^{44,52} $\text{TlBaSrCaCu}_2\text{O}_{6+\delta}$ (CD-Tl1212),²⁰ $(\text{Tl}_{1-x}\text{Pb}_x)\text{Ba}_2\text{CuO}_{5-\delta}$ (CD-Tl1201)⁵³ and CD-Hg1212³⁶ as CD-HTS's, and the purely oxygen-doped samples such as $\text{Bi}_2\text{Sr}_2\text{CaCu}_2\text{O}_{8+\delta}$ (OD-

Bi2212),¹⁸ OD-Hg1201,^{14,15} OD-Hg1212^{35,49} and OD-Tl2201^{18,53} as OD-HTS's. For comparison, the $\tau_c(T_c)$ vs p_u curve of OD-Y123 reported in Ref. 9 is also plotted in Fig. 5(b). The $T_c^{max.}$ and $P_{pl}^{opt.}$ are summarized in the Table I. The CD-HTS's follow the present asymmetric half-bell-shaped T_c -curve. The $\tau_c(T_c)$ vs p_u curve of the single-layer OD-Tl2201, which behaves differently from that of others in the plot of T_c vs P_{3D} as shown in Fig. 1(b),⁸ actually follows the asymmetric half-bell shaped T_c -curve. The other overdoped OD-HTS's also follow the half-bell-shaped T_c -curve. Note that the T_c of the underdoped OD-HTS is slightly enhanced from the half-bell shaped T_c -curve and T_c appears at a lower p_u . The OD-Y123 also shows the similar trend, although it is influenced by the CuO chain ordering.⁹ We attribute this to the influence of the soft oxygen dopants.⁵⁴ Thus, opposite to the common belief, the $\tau_c(T_c)$ vs p_u phase diagram of the majority of HTS's follow the asymmetric half-bell shaped T_c -curve. Noticed that the asymmetric half-bell-shaped T_c -curve goes to zero at $p_u \sim 1.3$. It is interesting to point out that if we take P_{pl}^{opt} to be universally equal to 0.16, as assumed in the P_{Tc} -scale, then the critical $p_u \sim 1.3$ corresponds to $P_{Tc} \sim 0.2$ in the P_{Tc} -scale. This value is very close to the proposed QCP ($P_{Tc} = 0.19$) identified by various experiments on the P_{Tc} -scale.^{1,6} Therefore this critical doping concentration is not located inside the superconducting dome and, physically, it is the doping concentration where all the phenomenology of high- T_c ceases to exist and the ground state becomes a conventional Fermi Liquid (FL) for $p_u > 1.3$.

In the overdoped triple-layer HTS, the charge density of the inner and outer planes were reported to be inhomogeneous.⁵⁵ This is consistent with the $\tau_c(T_c)$ vs p_u behavior of Bi₂Sr₂Ca₂Cu₃O_{8+ δ} (OD-Bi2223), black triangles in Fig. 5(b), that the T_c shows a flat region in the overdoped regime.⁵⁶ However, the $\tau_c(T_c)$ vs p_u behaviors of (Cu_{1-x}Ca_x)Ba₂Ca₂Cu₃O_{8+ δ} (CD-CuCa1223),⁵⁷ and (Cu_{1-x}C_x)Ba₂Ca₂Cu₃O_{8+ δ} (CD-CuC1223)⁵⁷ plotted into Fig. 5(a) show the same trend as that of the single- and double-layer CD-HTS's. The $\tau_c(T_c)$ vs p_u of overdoped TlBa₂Ca₂Cu₃O_{8+ δ} (OD-Tl1223),⁵⁸ and underdoped OD-Hg1223^{35,59} plotted in Fig. 5(b) also show the identical trend as that of the single- and double-layer OD-HTS's. Accordingly, although counter-intuitive, the charge density of the inner and outer planes of these materials is expected to be the same.

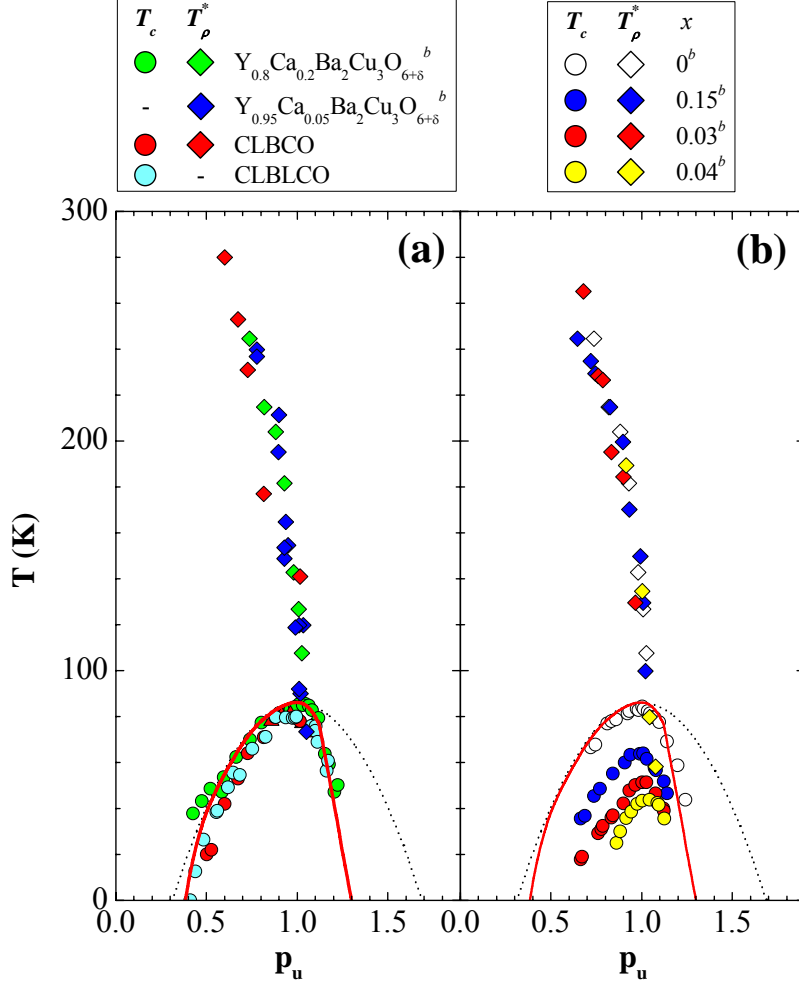


FIG. 4. T_c and resistive pseudogap temperature (T_ρ^*) as a function of p_u for (a) the $\text{YBa}_2\text{Cu}_3\text{O}_y$ -related materials and (b) $\text{Y}_{0.8}\text{Ca}_{0.2}\text{Ba}_2(\text{Cu}_{1-x}\text{Zn}_x)_3\text{O}_{6+\delta}$. In Fig. 4(a), the plotted data were cited from Refs. 6^b,43,44 for $\text{Y}_{1-x}\text{Ca}_x\text{Ba}_2\text{Cu}_3\text{O}_{6+\delta}$ (CD-Y123), Ref. 45 for $(\text{Ca}_{0.4}\text{La}_{0.6})(\text{Ba}_{1.35}\text{La}_{0.65})\text{Cu}_3\text{O}_{6+\delta}$ (CLBLCO) and Ref. 46 for $\text{CaLaBaCu}_3\text{O}_{6+\delta}$ (CLBCO). In Fig. 4(b), the plotted data were cited from Ref. 6^b for $\text{Y}_{0.8}\text{Ca}_{0.2}\text{Ba}_2(\text{Cu}_{1-x}\text{Zn}_x)_3\text{O}_{6+\delta}$. The solid line is a half-bell-shaped T_c -curve with $T_c^{\max} = 86$ K. The dotted line comes from the equation (1) with $T_c^{\max} = 86$ K.

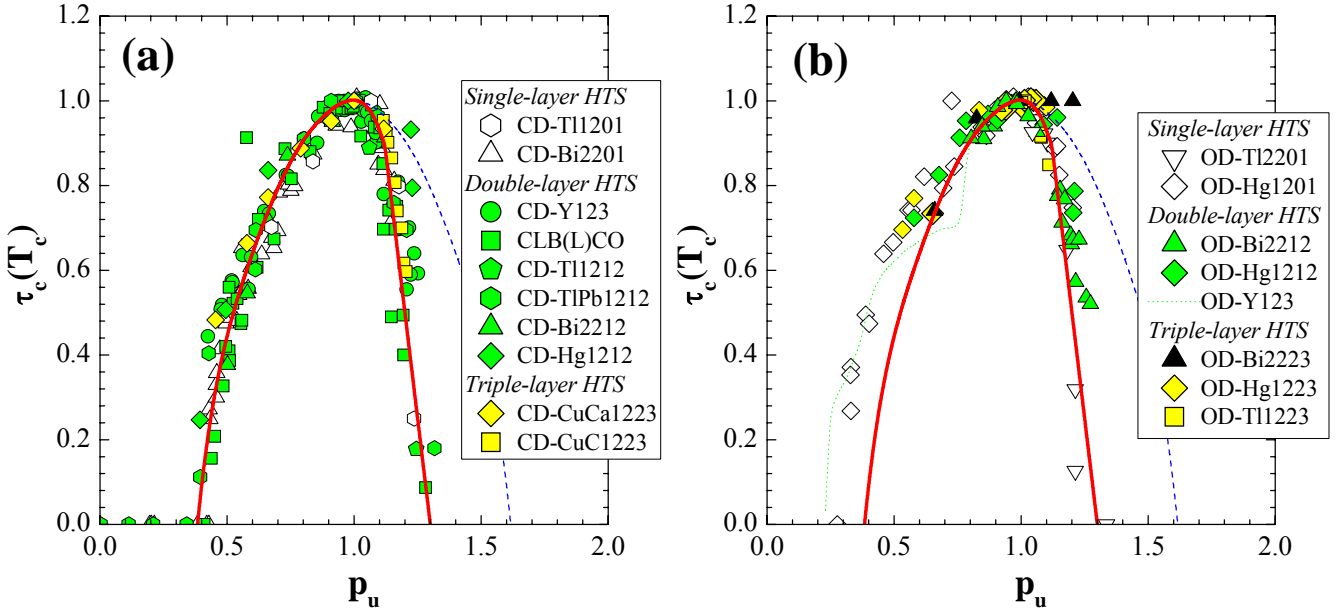


FIG. 5. Extended unified electronic phase diagram plotted as $\tau_c(T_c)$ vs p_u for (a) the cation and oxygen co-doped HTS's and (b) the purely oxygen doped HTS. For the CD-HTS, the plotted data were cited from Refs. 16 and 17 for CD-Bi2201, Ref. 53 for $(\text{Tl}_{1-x}\text{Pb}_x)\text{Ba}_2\text{CuO}_{5-\delta}$ (CD-Tl1201), Refs. 6^b,43,44,48 for CD-Y123, Ref. 45 for CLBLCO, Ref. 46 for CLBCO, Refs. 50 and 51 for $\text{Bi}_2\text{Sr}_2\text{Ca}_{1-x}\text{Y}_x\text{Cu}_2\text{O}_{8+\delta}$ (CD-Bi2212), Refs. 44 and 52 for $\text{Tl}_{1-x}\text{Pb}_x\text{Sr}_2\text{Ca}_{1-y}\text{Y}_y\text{Cu}_2\text{O}_{6+\delta}$ (CD-TlPb1212), Ref. 20 for $\text{TlBaSrCaCuO}_{6+\delta}$ (CD-Tl1212), Ref. 36 for CD-Hg1212, Ref. 57 for $(\text{Cu}_{1-x}\text{Ca}_x)\text{Ba}_2\text{Ca}_2\text{Cu}_3\text{O}_{8+\delta}$ (CD-CuCa1223) and $(\text{Cu}_{1-x}\text{C}_x)\text{Ba}_2\text{Ca}_2\text{Cu}_3\text{O}_{8+\delta}$ (CD-CuC1223). For the OD-HTS, the plotted data were cited from Refs. 14 and 15 for OD-Hg1201, Refs. 18 and 19 for OD-Tl2201, Res. 18 for $\text{Bi}_2\text{Sr}_2\text{CaCu}_2\text{O}_{6+\delta}$ (OD-Bi2212) and Refs. 35 and 49 for OD-Hg1212, Ref. 56 for $\text{Bi}_2\text{Sr}_2\text{Ca}_2\text{Cu}_3\text{O}_{8+\delta}$ (OD-Bi2223), Ref. 58 for $\text{TlBa}_2\text{Ca}_2\text{Cu}_3\text{O}_{6+\delta}$ (OD-Tl1223), and Refs. 35 and 59 for $\text{HgBa}_2\text{Ca}_2\text{Cu}_3\text{O}_{8+\delta}$ (OD-Hg1223). The solid and broken lines are an asymmetric half-bell-shaped T_c -curve and our superconducting dome, respectively. The dotted line is the T_c -curve for OD-Y123.⁹

Table 1. The $T_c^{max.}$ and $P_{pl}^{opt.}$ for the materials plotted in Figs. 5(a) – (b).

Material		T_c^{max} (K)	$P_{pl}^{opt.}$	Reference
Tl _{1-x} Pb _x Sr ₂ CuO _{5-δ}	(CD-Tl1201)	50	0.25	53
Bi ₂ Sr _{2-x} La _x CuO _{6+δ}	(CD-Bi2201)	36	0.28	16
Bi ₂ Sr _{2-x} La _x CuO _{6+δ}	(CD-Bi2201)	33	0.28	17
Y _{0.8} Ca _{0.2} Ba ₂ Cu ₃ O _{6+δ}	(CD-Y123)	85	0.237	43,48
Y _{0.8} Ca _{0.2} Ba ₂ Cu ₃ O _{6+δ}	(CD-Y123)	81	0.25	6 ^b
Y _{0.8} Ca _{0.2} Ba ₂ Cu ₃ O _{6+δ}	(CD-Y123)	85.5	0.238	44
(Ca _{0.4} La _{0.6})(Ba _{1.35} La _{0.65})Cu ₃ O _{6+δ}	(CLBLCO)	81	0.235	45
CaLaBaCu ₃ O _{6+δ}	(CLBCO)	81	0.232	46
(Tl _{0.5} Pb _{0.5})Sr ₂ Ca _{1-y} Y _y Cu ₂ O _{6+δ}	(CD-TlPb1212)	- ^c	0.25	44
Tl _{0.5+x} Pb _{0.5-x} Sr ₂ Ca _{1-y} Y _y Cu ₂ O _{6+δ}	(CD-TlPb1212)	94	0.235	52
Tl(BaSr)CaCu ₂ O _{6+δ}	(CD-Tl1212)	90	0.235	20
Bi ₂ Sr ₂ (Ca _{1-x} Y _x)Cu ₂ O _{8+δ}	(CD-Bi2212)	92	0.236	50
Bi ₂ Sr ₂ (Ca _{1-x} Y _x)Cu ₂ O _{8+δ}	(CD-Bi2212)	81	0.238	51
(Hg _{0.5} Fe _{0.5})Ba ₂ (Ca _{1-x} Y _x)Cu ₂ O _{6+δ}	(CD-Hg1212)	73	0.227	36
(Cu _{1-x} Ca _x)Ba ₂ Ca ₂ Cu ₃ O _{8+δ}	(CD-CuCa1223)	122	0.248	57
(Cu _{1-x} C _x)Ba ₂ Ca ₂ Cu ₃ O _{8+δ}	(CD-Cu1223)	110	0.215	57
Tl ₂ Ba ₂ CuO _{6+δ}	(OD-Tl2201)	93 ^d	0.25 ^d	18,21,53
HgBa ₂ CuO _{4+δ}	(OD-Hg1201)	97	0.235	14,15
Bi ₂ Sr ₂ CaCu ₂ O _{8+δ}	(OD-Bi2212)	92	0.238	18
HgBa ₂ CaCu ₂ O _{8+δ}	(OD-Hg1212)	127	0.227	35
HgBa ₂ CaCu ₂ O _{8+δ}	(OD-Hg1212)	125	0.227	49
Bi ₂ Sr ₂ Ca ₂ Cu ₃ O _{8+δ}	(OD-Bi2223)	108	0.215	56
HgBa ₂ Ca ₂ Cu ₃ O _{8+δ}	(OD-Hg1223)	135	0.215	35
HgBa ₂ Ca ₂ Cu ₃ O _{8+δ}	(OD-Hg1223)	138	0.215	59
TlBa ₂ Ca ₂ Cu ₃ O _{8+δ}	(OD-Tl1223)	128	0.23	58

^c The $T_c/T_c^{max.}$ was reported.

^d We use the reported highest $T_c = 93$ K as $T_c^{max.}$.²¹ From the plot of T_c vs P_{pl} in Fig. 1(a), the optimal P_{pl} is estimated to be ~ 0.25 . The detail is in the text.

C. Unified Electronic Phase Diagram (“UEPD”)

We now exam various characteristic temperatures and energies for HTS materials that fall into the asymmetric half-bell-shaped T_c phase diagram. $T_c(P_{pl})$ depends on the CuO_2 layer number, while the $T^*(P_{pl})$ is independent of the layer number.⁷ Therefore, we group the single- and double-layer HTS’s with similar $T_c^{max} \sim 90$ K together. The pseudogap is generally observed as the characteristic temperature (T^*) derived by a scaling of the temperature dependence, as a distinct change in the slope of the temperature dependence or as a peak value in the energy-dispersion at a fixed temperature. Therefore, a precise estimation can only be achieved through using a wide temperature or energy range. We only plot the characteristic temperatures and energies obtained by direct observation or those obtained through elaborated analysis of the data with the wide temperature or energy range.

We found in Ref. 7 that the various characteristic temperatures or pseudogap temperatures can be separated into two groups of the lower pseudogap temperature (T_{lp}^*) and upper pseudogap temperature (T_{up}^*). The T_c and major characteristic temperatures, including T_{lp}^* and T_{up}^* , are plotted on the reduced temperature-scale as a function of p_u in Figs. 6(a), (c) and (e). The characteristic energies such as the peak and hump energies observed in angle-resolved photoemission spectroscopy (ARPES) and tunneling, the coherent and two-magnon peaks observed in electronic Raman scattering (ERS) are plotted on a reduced energy-scale $\mu_c(E) \equiv E/k_B T_c^{max}$, where k_B is Boltzmann’s constant, as a function of p_u in Figs. 6(b), (d) and (f). We will call the four solid curves from top to bottom the hump temperature T_{hump}^* , T_{up}^* , T_{lp}^* and T_c -curves in the temperature-scale, and the hump energy (E_{hump}^*), the upper pseudogap energy (E_{up}^*), the lower pseudogap energy (E_{lp}^*) and Δ_c -curves in the energy-scale, respectively. The E_{hump}^* , T_{up}^* , T_{lp}^* and T_c -curves are directly determined from the plotted data. The T_{hump}^* , E_{up}^* , E_{lp}^* and Δ_c -curves are converted from the E_{hump}^* , T_{up}^* , T_{lp}^* and T_c -curves using a relation of $T = E/zk_B$ or $E = zk_B T$ for each characteristic energy or temperature. In the energy-scale, the solid curves correspond to $z = 3.5$ and gray zone shows the energy range from $3k_B T$ to $4k_B T$. Firstly, we summarize the characteristic temperatures and energies derived from the transport and thermodynamic properties in figures 6(a) and (b). Here, the T^* was determined from

the resistivity (ρ),^{6b,14,46,47a,60-62a} c -axis resistivity (ρ_c),^{62-64a} TEP ,^{14,18,44-46,50,65} specific heat^{66a} and femtosecond quasiparticle relaxation (QPR) experiments.^{67a} The T^* 's from ρ and ρ_c are temperatures where the T -linear ρ and ρ_c in the high temperature bend downward, respectively. The T^* 's from TEP and specific heat are the temperatures where the TEP or the electronic specific heat coefficient exhibits a maximum value in the temperature dependence. The T^* 's determined from the TEP and specific heat measurements lie on the T_{lp}^* -curves, while the T^* 's determined from the ρ and QPR lie on the T_{up}^* -curves, as reported in Ref. 7. Accordingly, the upper pseudogap is identified by the ρ and QPR, and the lower pseudogap is identified by the TEP and specific heat experiments. But, the T^* determined from the ρ_c tends to be higher than the T_{up}^* ($> T_{lp}^*$), although the doping range is restricted. This may suggest a third pseudogap as already pointed out in Ref. 7. This suggestion is further supported by the similar behavior derived by other probes in the temperature- and energy-scales. Recently the resistivity curvature mapping based on the data of in-plane resistivity up to 300 K showed that there are two inflection points, the upper inflection point and the lower inflection point, identified in the ρ vs T curve far above T_c .^{123a} We plot the upper inflection point as the triangle and the lower inflection point as the inverted triangle of OD-Y123 into the Fig. 6(a). The lower and upper inflection points seem to be corresponding to the T_{lp}^* - and T_{up}^* -curves, respectively.

For the characteristic energies, we use the data reported in the specific heat,^{68a,69a,70b} thermal conductivity studies,^{71-73a} and QPR experiment.^{67a,74a} The E^* 's determined from the QPR lie on the E_{up}^* -curve. The E^* 's determined from the thermal conductivity show up on either E_{lp}^* or E_{up}^* curve. In the overdoped side, these E^* 's clearly merge into the Δ_c -curve. This indicates that there is no QCP inside the superconducting dome. In Fig. 6(b), the normal state gap, $E_{sh}^*(110\text{ K})$ and zero temperature superconducting gap, $E_{sh}^*(0\text{ K})$ determined by the specific heat measurement are plotted as the open symbols and solid circles, respectively.^{68-70a} The $E_{sh}^*(110\text{ K})$ at $p_u < 0.85$ and $E_{sh}^*(0\text{ K})$ follows the E_{lp}^* - or $zk_B T_{lp}^*$ -curve. But, the $E_{sh}^*(110\text{ K})$ at $p_u > 0.85$ deviates downward from the E_{lp}^* -curve, crosses the Δ_c -curve and finally goes to zero inside the Δ_c -curve. The temperature of $\sim 110\text{ K}$ ($\tau_c(110\text{ K}) = 110/90 \sim 1.2$) is corresponding to the lower pseudogap temperature at $p_u \sim 0.85$. The influence of the lower pseudogap on the extraction of the E^* 's is clearly seen.

The plotted E_{sh}^* (110K) is the same data set used to support the existence of the QCP *inside* the superconducting dome on the P_{T_c} -scale.¹ Accordingly, the existence of the QCP inside the superconducting dome is extrinsic to high- T_c .

We summarize the characteristic temperatures and energies derived from the spectroscopic measurements in Figs. 6(c) and (d). The T^* determined in the angle-integrated photoemission spectroscopy (AIPES) lies on the T_{hump}^* .^{75a} The T^* determined from the ARPES,^{76-78a} and superconductor-insulator-superconductor (SIS) tunneling spectroscopy^{79a} can not be grouped into either T_{up}^* or T_{lp}^* -curve, since they lie between the T_{up}^* - and T_{lp}^* -curves. The E^* determined in the ARPES,^{77a,78a,80-84a} and tunneling,^{79a,85-90a} are plotted in Fig. 6(d): the peak and hump energies observed in ARPES and tunneling lie on the E_{lp}^* and E_{hump}^* curves, respectively. It is clearly seen that there is a third energy scale corresponding to the hump structure observed in the ARPES and tunneling spectroscopy.

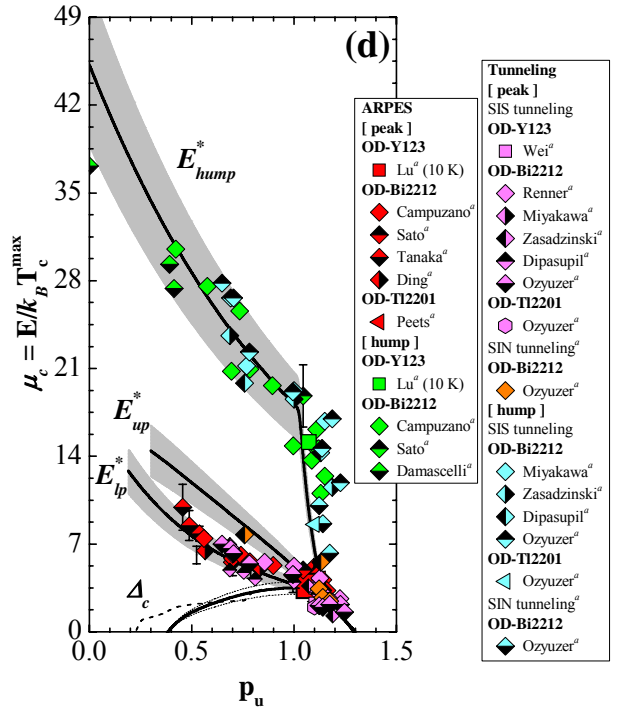
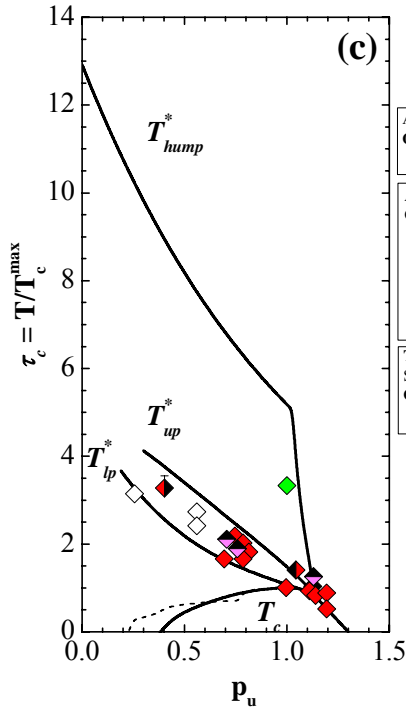
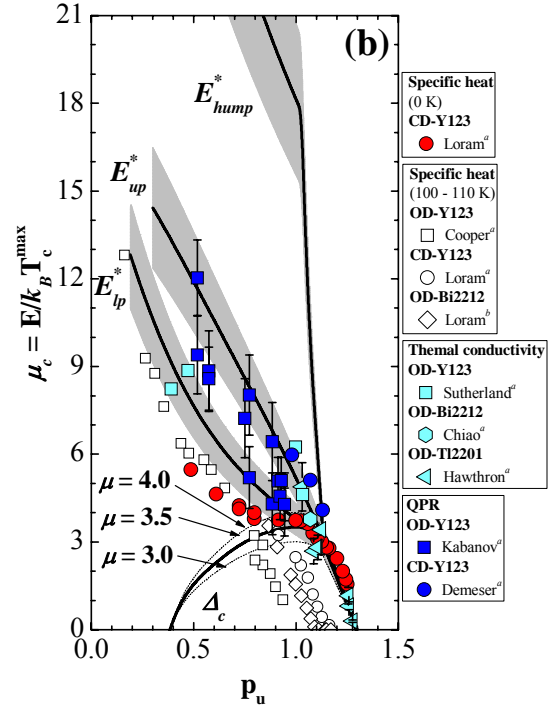
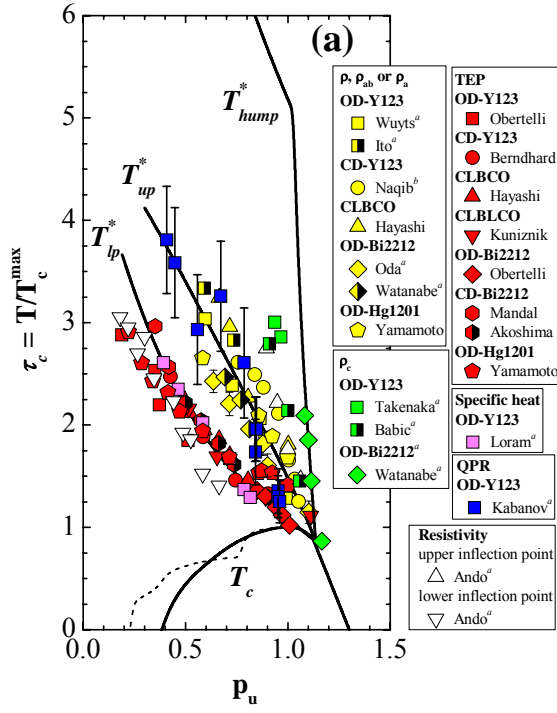
We summarize the characteristic temperatures and energies derived from the spin and charge probes in Figs. 6(e) and (f), respectively. The T^* was observed in the spin-lattice relaxation rate deviated from temperature dependence of the nuclear magnetic resonance (NMR) $((T_1T)^{-1})$,^{91-94a} NMR Knight shift parallel to c -axis (K_c),^{91a,92a} neutron scattering,^{95a,96a} and susceptibility (χ).^{61a,62a,97a} The characteristic energies are extracted from the ERS,^{98-108a} and neutron scattering.^{96a} For the characteristic temperatures, the T^* determined from the $(T_1T)^{-1}$ lies on the T_{lp}^* . The T^* determined from the neutron lies between T_{up}^* - and T_{lp}^* -curves. The T_{mK}^* and T_K^* observed in K_c lie on the T_{hump}^* and T_{up}^* , respectively. Here, T_{mK}^* is a temperature where the constant K_c at high temperature bends downward, and T_K^* is a temperature where the linear K_c below T_{mK}^* bends downward.^{91a,92a} For the characteristic energies, the half of the coherent peak energy of B_{2g} ERS,^{102,103,107-110a} the half of the coherent peak energy of B_{1g} ERS,^{98-110a} and the half of the two-magnon peak energy of B_{1g} ERS^{99a,103a,104a} lie on the Δ_c , E_{lp}^* and E_{hump}^* -curves, respectively.

From Figs. 6(a) – (f) we can conclude that the phase diagram fundamentally reproduce the T vs P_{pl} plot in Ref. 7. Their characteristic temperatures T^* lie on either the T_{up}^* or the T_{lp}^* curve in Ref. 7. Furthermore, the third characteristic energy, the ‘‘hump’’ energy, does exist, although it is hard to detect as the corresponding characteristic

temperature or T_{hump}^* . All four characteristic temperatures (T_c , T_{lp}^* , T_{up}^* and T_{hump}^*) and corresponding energies (Δ_c , E_{lp}^* , E_{up}^* and E_{hump}^*) do not cross each other. The four temperatures and energies tend to converge with increasing p_u , merge at $p_u \sim 1.1$ and finally vanish at $p_u \sim 1.3$.

Some T^* 's (E^* 's) have relatively large scattering, and is hard to group into either T_{up}^* (E_{up}^*)-curve or T_{lp}^* (E_{lp}^*)-curve. For example, the E^* from the thermal conductivity and the T^* from the ARPES, tunneling spectroscopy and neutron scattering are scattered. These scattering may come from the differences in the characteristic time-scale and length-scale specific to different experimental probes for observing the intrinsically inhomogeneous electronic states, as discussed by D. Mihailovic and V.V. Kabanov.¹¹¹ Indeed, similar to T_{up}^* - and T_{lp}^* -curves or E_{up}^* - and E_{lp}^* -curves, they all become smaller and closer in the magnitude with increasing doping in the underdoped regime. They merge into T_c or Δ_c -curve in the overdoped regime and universally vanish at $p_u=1.3$. The pseudogap, manifested either as the characteristic energy or characteristic temperature and independent of its origin, universally disappears at $p_u \sim 1.3$ together with the superconductivity. This strongly suggests that the pseudogap phase is the precursor of the superconducting phase.

In Fig. 8(a), we present a sketch of the unified electronic phase diagram for HTS's based purely on experimental grounds. The characteristic features of the unified electronic phase diagram for single- and double-HTS's with $T_c^{max} \sim 90$ K are: (i) the asymmetric half-bell-shaped T_c -curve (SC phase), (ii) there are three characteristic temperatures, T_{hump}^* , T_{up}^* and T_{lp}^* in the underdoped region ($p_u < 1$), (iii) all three characteristic temperatures and T_c come together at $p_u = 1.1$ in the overdoped region and vanish at $p_u = 1.3$, (iv) the T_{hump}^* changes into the rapid decrease at $p_u \sim 1$, (v) the T_{hump}^* and T_{lp}^* are concave upward, while the T_{up}^* is concave downward, and (vi) the electronic phase diagram on the temperature-scale can be translated into that on the energy-scale through $E = zk_B T$ with $z = 3.5 \pm 0.5$. Although we use the HTS materials with $T_c^{max} \sim 90$ K as our model system, we should emphasize that (i) – (vi) are salient features for all, except of SrD-La214 discussed in the next section, HTS's. We will call this phase diagram the ‘‘Unified Electronic Phase Diagram (UEPD)’’ of HTS. Finally the T_{lp}^* - and T_{up}^* -curves tend to merge into the Néel temperature (T_N) curve with undoping.^{126,127}



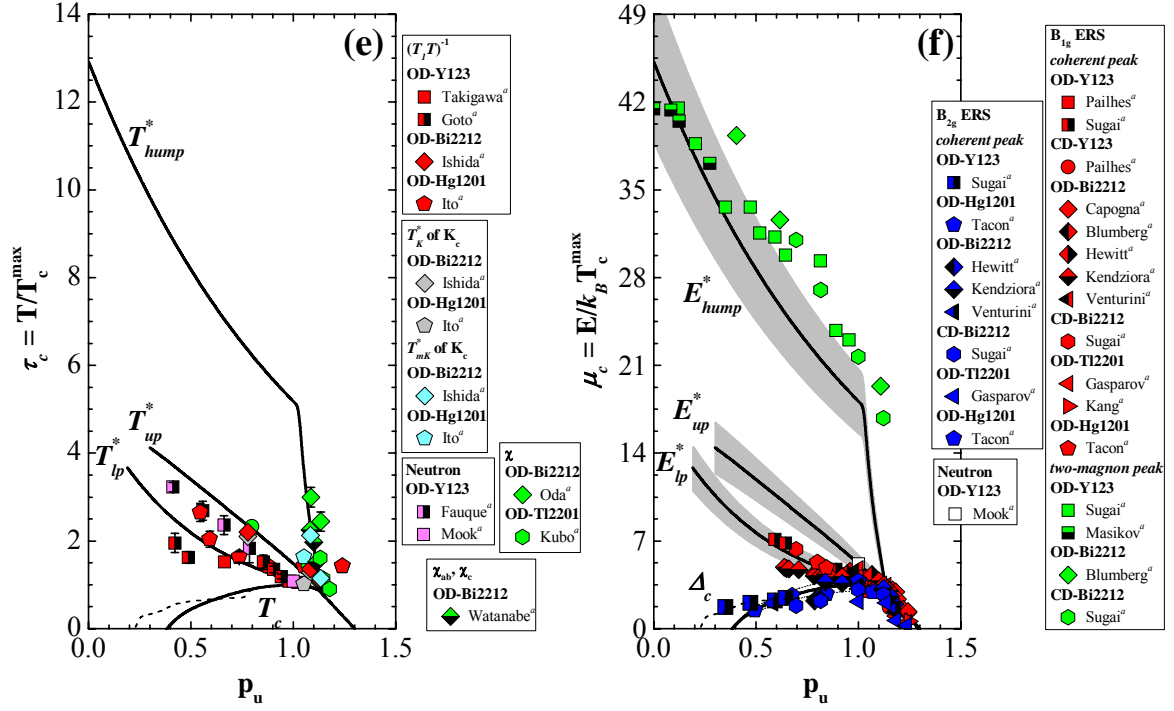


FIG. 6. Unified electronic phase diagram for the single- and double-layer HTS with $T_c^{\max} \sim 90$ K. The temperature- and energy-scale for the pseudogap and superconducting gap obtained from transport properties are summarized in Figs. 6(a) and (b), from the spectroscopy properties in Figs. 6(c) and (d), and from NMR, QPR and scattering properties in Figs. 6(e) and (f), respectively. For Fig. 6(a), the T^* were cited from Ref. 6^b, 14,46, 47^a,60-62^a for the ρ , Refs. 14,18,44-46,50,65 for the TEP , Refs. 62-64^a for the ρ_c , and Ref. 66^a for the specific heat, respectively. The two inflection points come from Ref. 123^a. For Fig. 6(b), the energy-scale was cited from Refs. 68-70^a for the specific heat, Refs. 71-73^a for the thermal conductivity, and Refs. 67^a and 74^a for the QPR. For Fig. 6(c), the T^* were cited from Refs. 76-78^a for the ARPES, Ref. 75^a for the AIPES, and Refs. 62^a and 79^a for the superconductor-insulator-superconductor (SIS) tunneling. For Fig. 6(d), the energy-scale was cited from Refs. 77^a,78^a,80-84^a for the ARPES and Refs. 79^a and 85-90^a for the SIS and SIN (N: normal metal) tunneling. For Fig. 6(e), the T^* was cited from Refs. 61^a,62^a,97^a for the susceptibility, Refs. 60^a and 91-94^a for the NMR, Refs. 95^a and 96^a for the neutron scattering, and Refs. 91^a and 92^a for K_c . For Fig. 6(f), the energy-scale was cited from Refs. 98-110^a for the ERS, and Ref. 96^a for the neutron scattering. The E_{hump}^* , T_{up}^* , T_{lp}^* and T_c -curves are directly determined from the plotted data. The T_{hump}^* , E_{up}^* , E_{lp}^* and Δ_c -curves are calculated from the E_{hump}^* , T_{up}^* , T_{lp}^* and T_c -curves using a relation of $E = zk_B T$, respectively. The broken lines show the T_c -curve or Δ_c -curve the for OD-Y123. In the energy-scale, the solid lines corresponds to $z = 3.5$ and gray zone shows the energy range from $3k_B T$ to $4k_B T$. The upper and lower dotted lines correspond to $z = 4$ and 3 , respectively.

D. Phase Diagram for SrD-La214

Now we discuss the HTS with symmetric T_c -curve, the phase diagram of SrD-La214. For the SrD-La214, the characteristic temperatures on the reduced temperature-scale and characteristic energies on the reduced energy-scale are plotted as a function of p_u in figures 7(a) and (b), respectively. The data on the temperature-scale come from the TEP ,^{13,25,26,69} susceptibility,¹¹²⁻¹¹⁵ resistivity,^{112,116} ARPES,¹¹⁷⁻¹¹⁹ AIPES,¹²⁰ QPR,¹²¹ specific heat,⁴⁸ and NMR.¹²² The data on the energy-scale come from ARPES,¹¹⁷⁻¹¹⁹ AIPES,¹²⁰ QPR,¹²¹ specific heat,⁴⁸ NMR,¹²² and ERS.¹⁰³ Firstly, noticed that the characteristic temperatures are separated into not three curves of T_{lp}^* , T_{up}^* and T_{hump}^* , but two curves. Also in the energy-scale, the characteristic energies are separated into two curves. In the *UEPD* the T_{lp}^* - or E_{lp}^* - curve was defined by the TEP , the peak structure of ARPES and tunneling, specific heat, and NMR, and the T_{hump}^* - or E_{hump}^* - curve was defined by the ρ_c , *susceptibility*, the hump structure of ARPES and tunneling, and two-magnon peak of B_{1g} ERS. In the SrD-La214, the lower curve of the temperature- or energy-scale is identified by the TEP , the peak structure of ARPES and tunneling, specific heat, and NMR, and the upper curve is identified by the susceptibility, the hump structure of ARPES and tunneling, two-magnon peak of B_{1g} ERS. Accordingly, the lower and upper curves of SrD-La214 are designated to be T_{lp}^* and T_{hump}^* (E_{lp}^* and E_{hump}^*), respectively. In the SrD-La214, the T^* or E^* defined by the resistivity and QPR lie on either of the two curves, suggesting no T_{up}^* - or E_{up}^* -curve. Because, in the *UEPD*, the T^* or E^* defined by the ρ and QPR lied on the T_{up}^* - or E_{up}^* - curve. In fact, the T_ρ^* for the SrD-La214 with $x < 0.16$ ($p_u < 1$) lie on the T_{hump}^* -curve,¹¹² while the T_ρ^* for $x > 0.14$ ($p_u > 0.875$) lie on the T_{lp}^* -curve.¹¹⁶ We also plot the upper and lower inflection points of the in-plane resistivity into the Fig. 7(a).¹²³ The upper and lower inflection points seem to be corresponding to the T_{hump}^* - and T_{lp}^* -curves, respectively. In the SrD-La214, the usual upper pseudogap temperatures identified in *UEPD* tend to lie on either lower pseudogap temperature or the hump temperature.

In Fig. 8(b), we present a sketch of the phase diagram for SrD-La214. The $T_c(p_u)$ follows a symmetric bell-shaped T_c -curve (SC phase). This is quite different from the feature (i) of the *UEPD*. There are two characteristic temperatures, T_{hump}^* and T_{lp}^* in the

range from the underdoped regime. This is also different from the feature (ii) above. The T_{lp}^* of SrD-La214 seems to be a combination of T_{up}^* and T_{lp}^* of the UEPD. Although the T_c , T_{hump}^* and T_{lp}^* decreases with doping, there is no merging until the end point. This is also different from the feature (iii) above. The T_c , T_{hump}^* and T_{lp}^* fall down to $(p_u, \tau_c) = (1.6, 0)$ in contrast to $(1.3, 0)$ in the UEPD. There is a slight change in curvature in $T_{hump}^*(p_u)$ at $p_u \sim 1$. This may share the same origin as the feature (iv) above, although it is much weaker in the SrD-La214 system. Both the features (v) and (vi) are similar to that of UEPD.

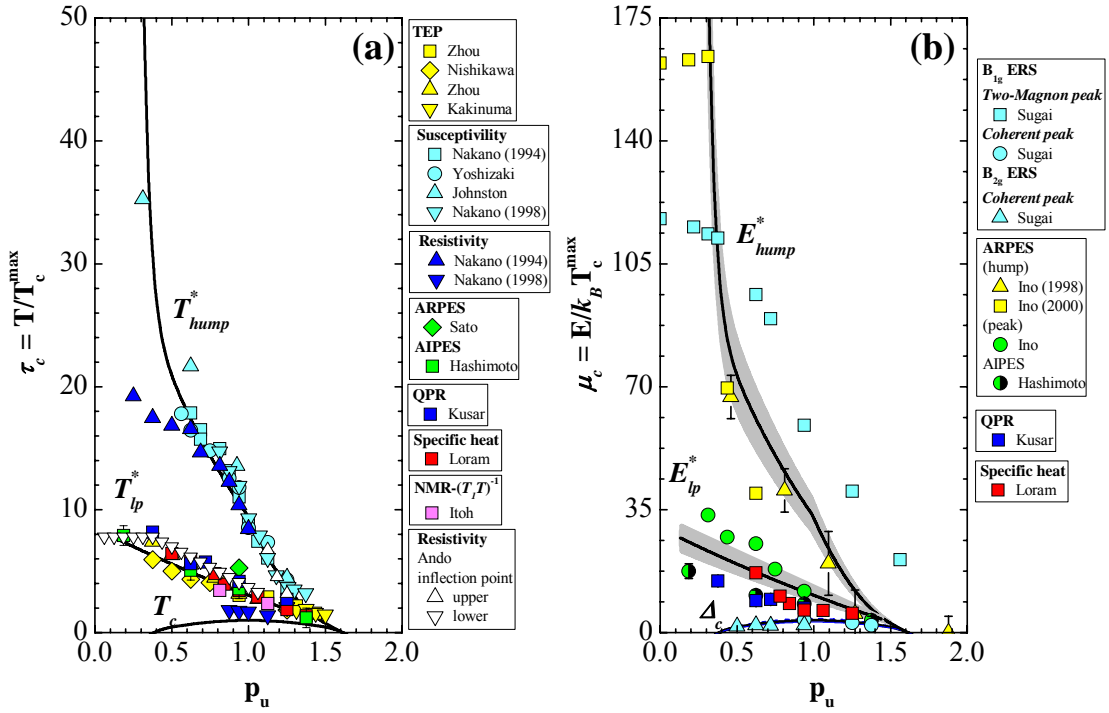


FIG. 7. Electronic phase diagram for the single-layer SrD-La214. The temperature- and energy-scale for the characteristic temperatures and energies are summarized in Figs. 7(a) and 7(b), respectively. For Fig. 7(a), the T^* were cited from Refs. 13,25,26,69 for the *TEP*, from Refs. 112-115 for the susceptibility, from Refs. 112 and 116 for the resistivity, from Ref. 120 for the AIPES, from Ref. 121 for the QPR, from Refs. 117-119 for the ARPES, from Ref. 103 for the ERS, from Ref. 122 for the NMR, and from Ref. 48 for the specific heat. The two inflection points come from Ref. 123. For Fig. 7(b), the data for the energy-scale were cited from Ref. 103 for the ERS, from Refs. 118 and 119 for the ARPES, from Ref. 120 for the AIPES, from Ref. 121 for the QPR, and from Ref. 48 for the specific heat.

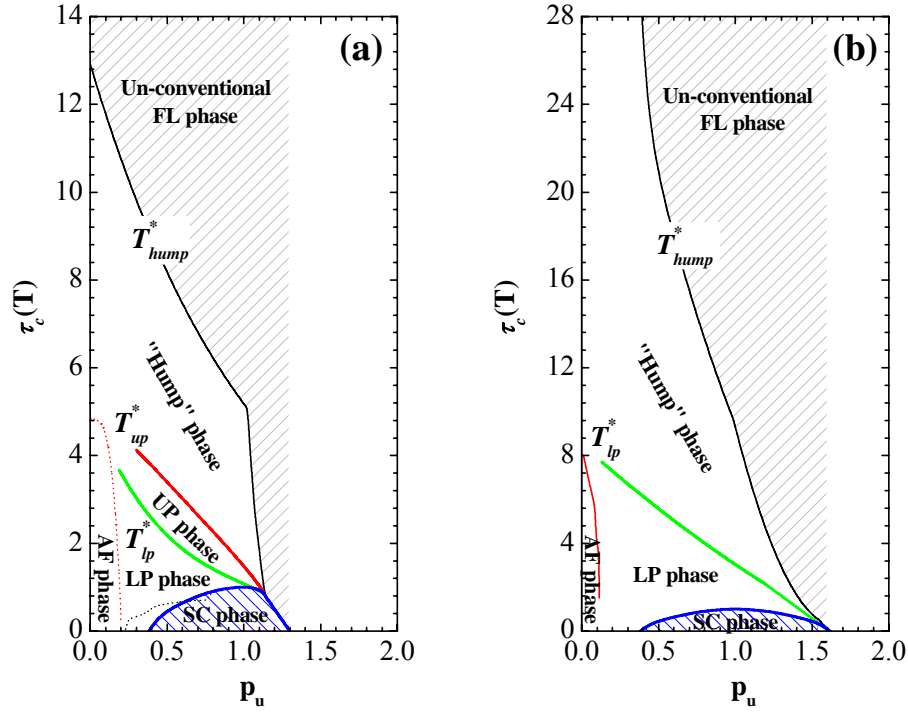


FIG. 8. Sketches of (a) the UE PD for the HTS with $T_c^{max} \sim 90$ K and (b) the phase diagram for the SrD-La214. The superconducting (SC) and antiferromagnetic (AF) phases represented by the dotted lines are coming from OD-Y123.^{9,125} The AF phase is cited from Refs. 126 and 127.

E. Comparison among the UEPD and the Other Phase Diagrams

The present UEPD is different from the phase diagrams that were proposed and discussed in Refs. 1-3 and 124. The phase diagram in Ref. 1 suggests that the single T^* -curve crosses the bell-shaped T_c -curve or superconducting dome at around the optimal doping level, and fall down to $T = 0$ at the QCP inside the superconducting dome. This phase diagram implies that there is no correlation between the pseudogap phase and high- T_c phase, and therefore the pseudogap is a pure competing order. The phase diagram of Ref. 2 suggests that the bell-shaped T_c -curve intercepts the double T^* -curves at around the optimal doping level. The upper and lower T^* -curves are concave downward and upward, respectively. These phase diagram is based on the P_{T_c} -scale, since the T_c follows the superconducting dome. The phase diagram on Ref. 3 shows a tendency that the double T^* -curves merge into the asymmetric T_c -curve at around the slightly overdoped level and go to zero with T_c at the end point. But, both T^* -curves are concave downward. In Refs. 1-3, the pseudogap does not merge into the T_N -curve with undoping. The phase diagram discussed in Ref. 124 shows that the single T^* -curve smoothly merges into the T_N -curve with undoping, and smoothly merges into the asymmetric T_c -curve at the end point with doping. But, the single T^* -curve is concave downward. Thus, without alluding to the microscopic picture for the high- T_c mechanism, all the previously proposed phase diagrams are different from our UEPD, except that the asymmetric T_c -curve in Refs. 3 and 124 is similar to the present half-bell shaped T_c -curve.

The present UEPD clearly shows that the pseudogap appears above T_c for $p_u < 1.1$ and for $p_u > 1.1$ pseudogap appears at T_c . Even experimental data that supported a QCP inside the superconducting dome on the P_{T_c} -scale followed the UEPD. The phase diagram for the SrD-La214 shows that pseudogap temperatures and corresponding characteristic energies always exist above the superconducting dome, until the pseudogap disappears together with the superconducting phase at $p_u = 1.6$. These results indicate that for all the HTS's the pseudogaps phase always co-exists with the superconducting phase up to the the end point and does not intersect the superconducting phase. Furthermore, the overdoped HTS with superconductivity cannot be regarded as a conventional Fermi liquid (FL) phase, since there is always the pseudogap phase with superconducting phase.

Both phase diagrams suggest no QCP inside the superconducting dome. Actually, it has reported that QCP may exist at the end point of the superconducting dome when superconductivity has completely disappeared in CLBLCO,¹²⁸ SrD-La214,¹²⁹ OD-Tl2201,¹³⁰ and OD-Bi2212.¹³⁰

The UEPD is consistent with the idea that the pseudogap phase is, if not sufficient, necessary for the high- T_c . It also implies that at least two distinct energy scales, pseudogap and superconductivity, are required to realize high- T_c . If we adopt a scenario that superconducting pairing is realized in the pseudogap phase and the global phase coherence occurs at T_c , then the smooth merging of T^* 's and T_c in the overdoped regime suggests that cuprates become a “more conventional” superconductor. Because pairing and phase coherence occurs at the same temperature (T_c). However since pseudogap still exists, it simply merges with T_c and changes with T_c , therefore the superconducting state as well as the normal state are still “unconventional” up to the end point as reported in some studies.^{72,83} This also explains why the pseudogap phase was never observed in the overdoped regime except SrD-La214. Even in the SrD-La214, the observation of the pseudogap in the overdoped regime strongly depends on the experimental probe. For example, it is not observed in the resistivity measurements but can be clearly seen by magnetic susceptibility and TEP measurements, as shown in Fig. 7.

In the previous paper, we pointed out that the observed T_{lp}^* and T_{up}^* are coming from not one pseudogap, but two pseudogaps.⁷ Because, the temperature where the TEP has the broad peak, corresponding to T_{lp}^* , was different from the temperature where the TEP starts to depend on the Zn-doping, corresponding to T_{up}^* .⁷ However, according to the idea by D. Mihailovic and V.V. Kabanov that,¹¹¹ we can not completely rule out a possibility that three characteristic temperatures, including T_{hump}^* , are of the same physical origin. The different characteristic temperatures may come from the differences in the characteristic time-scale and length-scale specific to different experimental probes for observing the intrinsically inhomogeneous electronic states or pseudogap phase.

IV. Summary

We have proposed a dimensionless hole-doping concentration (p_u), scaled by the optimal hole-doping concentration, for all HTS's and construct a unified electronic phase diagram (UEPD) for almost all HTS's, except of the purely cation-doped SrD-La214. In the UEPD all experimentally observed characteristic temperatures and energies converge as p_u increases in the underdoped regime, they merge together with the T_c vs p_u curve at $p_u \sim 1.1$ in the overdoped regime and finally goes to zero at $p_u \sim 1.3$. On the other hand, for SrD-La214, although all experimentally observed characteristic temperatures and energies converge as p_u increases in the underdoped regime, they merge together with the T_c vs p_u curve at $p_u \sim 1.6$ where T_c goes to zero. However, the detection of pseudogap becomes subtle and probe-dependent for $p_u > 1$. Both the UEPD and the phase diagram of SrD-La214 clearly show that the pseudogap phase is a precursor of high- T_c . Finally, there remains a question of why the phase diagram for SrD-La214 is different from the UEPD. The UEPD is based on the cation and oxygen co-doped HTS materials, while the SrD-La214 is the pure cation doped HTS. Although the pure oxygen-doped HTS also follows the UEPD, the phase diagram is slightly deformed by the influence of the thermally induced oxygen redistribution. Accordingly, although we can not pin down exactly why the SrD-La214 does not follow the UEPD, we speculate that the differences are coming from a combination of lattice response, such as octahedral tilt mode, to hole doping and the hard-dopant effect discussed in Ref. 54. Further studies are necessary to properly address this issue.

Acknowledgements

T.H. would like to thank Dr. M. Tanimoto of Asahikawa Medical College for offering relief-time for this study. This work was supported by the State of Texas through the Texas Center for Superconductivity at the University of Houston.

*Electronic address: homma@asahikawa-med.ac.jp

+ Electronic address : phor@uh.edu

References

- ¹ J.L. Tallon, Physica C **349** 53 (2001).
- ² B. Batlogg and V. J. Emery, Nature **382**, 20 (1996).
- ³ V. J. Emery, S. A. Kivelson and O. Zacher, Phys. Rev. B **56**, 6120 (1997).
- ⁴ J. B. Torrance, Y. Tokura, A. Nazzal, A. Bezinge, T. C. Huang and S. S. P. Parkin, Phys. Rev. Lett. **61**, 1127 (1988).
- ⁵ M. R. Presland, J. L. Tallon, R. G. Buckley, R. S. Liu and N. E. Flower, Physica C **176**, 95 (1991).
- ⁶ S. H. Naqib, J. R. Cooper, R. S. Isram and J. L. Cooper, Phys. Rev. B **71**, 184510 (2005) ; S. H. Naqib, Physica (Amsterdam) **433C**, 43 (2006).
- ⁷ T. Honma, P. H. Hor, H. H. Hsieh and M. Tanimoto, Phys. Rev. B **70**, 214517 (2004).
- ⁸ T. Honma and P. H. Hor, Supercond. Sci. Tech. **19**, 907 (2006).
- ⁹ T. Honma and P. H. Hor, Phys. Rev. B **75**, 012508 (2007).
- ¹⁰ P. G. Radaelli *et al.*, Phys. Rev. B **49**, 4163 (1994).
- ¹¹ T. Nagano, Y. Tomioka, Y. Nakayama, K. Kishio and K. Kitazawa, Phys. Rev. B **48**, 9689 (1993).
- ¹² S. Komiya, H. D. Chen, S. H. Zhang and Y. Ando, Phys.Rev.Lett. **94**, 207004 (2005).
- ¹³ N. Kakinuma, Y. Ono and Y. Koike, Phys. Rev. B **59**, 1491 (1999).
- ¹⁴ A. Yamamoto, W. Hu and S. Tajima, Phys. Rev. B **63**, 024504 (2000).
- ¹⁵ J. A. Willson and M. Farbod, Supercond. Sci. Tech. **13**, 307 (2000).
- ¹⁶ Y. Ando *et al.*, Phys. Rev. B **61**, 14956(R) (2000).
- ¹⁷ Y. Okada and H. Ikuta, Physica (Amsterdam) **445-448C**, 84 (2006).
- ¹⁸ S. D. Obertelli, J. R. Cooper and J. L. Tallon, Phys. Rev. B **46**, 14928 (1992).
- ¹⁹ L. Shu-Yuan *et al.*, Phys. Rev. B **47**, 8324 (1993).
- ²⁰ C. Martin, J. Hejtmanek, Ch. Simon, A. Maignan and B. Raveau, Physica (Amsterdam) **250C**, 235 (1995).
- ²¹ J. L. Wagner, O. Chmaissem, J. D. Jorgensen, D. G. Hinks, P. G. Radaelli, B. A. Hunter and W. R. Jensen, Physica (Amsterdam) **277C**, 170 (1997).

- ²² J. R. Cooper, B. Alavi, L. -W. Zhou, W. P. Beyermann and G. Grüner, *Phys. Rev. B* **35**, 8794 (1987).
- ²³ D. C. Johnston, J. P. Stokes, D. G. Goshorn and J. T. Lewandowski, *Phys. Rev. B* **36**, 4007 (1987).
- ²⁴ Y. Nakamura and S. Uchida, *Phys. Rev. B* **47**, 8369 (1993).
- ²⁵ T. Nishikawa, J. Takeda and M. Sato, *J. Phys. Soc. Jpn.* **63**, 1441 (1994).
- ²⁶ J. -S. Zhou and J. B. Goodenough, *Phys. Rev. B* **51**, 3104 (1995) ; **54**, 12488 (1996).
- ²⁷ Z. A. Xu, N. P. Ong, T. Kakeshita, H. Eisaki and S. Uchida, *Physica (Amsterdam)* **341-348C**, 1711 (2000).
- ²⁸ Y. Park, B. H. Kim, J. S. Kim, D. C. Kim and B. Kim, *J. Supercond.* **18**, 743 (2005).
- ²⁹ J. -S. Zhou and J. B. Goodenough, *Phys. Rev. B* **56**, 6288 (1997).
- ³⁰ J. D. Yu, Y. Inaguma, M. Itoh, M. Oguni and T. Kyômen, *Phys. Rev. B* **54**, 7445 (1996).
- ³¹ F. Devaux, A. Manthiram and J. B. Goodenough, *Phys. Rev. B* **41**, 8723 (1990).
- ³² A. J. Smits, W. J. Elion, J. M. van Ruitenbeek, L. J. de Jongh and W. A. Groen, *Physica (Amsterdam) C* **199**, 276 (1992).
- ³³ M. Ambai, Y. Kobayashi, S. Iikubo and M. Sato, *J. Phys. Soc. Jpn.* **71**, 538 (2002).
- ³⁴ J. Takeda, T. Inukai and M. Sato, *J. Phys. Soc. Jpn.* **69**, 2917 (2000).
- ³⁵ A. Fukuoka *et al.*, *Phys. Rev. B* **55**, 6612 (1997).
- ³⁶ E. Kandyle, *Physica (Amsterdam) C* **422** 102 (2005).
- ³⁷ A. Ino, C. Kim, M. Nakamura, T. Yoshida, T. Mizokawa, A. Fujimori, Z. -X. Shen, T. Kakeshita, H. Eisaki and S. Uchida, *Phys. Rev. B* **65**, 094504 (2002).
- ³⁸ T. Yosida, X. J. Zhou, K. Tanaka, W. L. Yang, Z. Hussain, Z. -X. Shen, A. Fujimori, S. Sahrakorpi, M. Lindroos, R. S. Markiewicz, A. Bansil, S. Komiyama, Y. Ando, H. Eisaki, T. Kakeshita and S. Uchida, *Phys. Rev. B* **74**, 224510 (2006).
- ³⁹ T. Kondo, T. Takeuchi, U. Mizutani, T. Yokoya, S. Tsuda and S. Shin, *Phys. Rev. B* **72**, 024533 (2005).
- ⁴⁰ M. Merz, N. Nücker, P. Schweiss, S. Schuppler, C. T. Chen, V. Chakarian, J. Freeland, Y. U. Idzerda, M. Kläser, G. Müller-Vogt and Th. Wolf, *Phys. Rev. Lett.* **80**, 5192 (1998).

- ⁴¹ H. Kotegawa, Y. Tokunaga, K. Ishida, G. -q. Zheng, Y. Kitaoka, H. Kito, A. Iyo, K. Tokiwa, T. Watanabe and H. Ihara, *Phys. Rev. B* **64**, 064515 (2001).
- ⁴² N. E. Hussey, M. Abdel-Jawad, A. Carrington, A. P. Mackenzie and L. Balicas, *Nature* **425**, 814 (2003).
- ⁴³ J. R. Cooper *et al.*, *Physica (Amsterdam)* **341-348C**, 855 (2000).
- ⁴⁴ C. Bernhard and J. L. Tallon, *Phys. Rev. B* **54**, 10201 (1996).
- ⁴⁵ A. Knizhnik *et al.*, *Physica (Amsterdam)* **321C**, 199 (1999).
- ⁴⁶ K. Hayashi *et al.*, *Czech. J. Phys.* **46** (S2), 1171 (1996).
- ⁴⁷ T. Ito, K. Takenaka and S. Uchida, *Phys. Rev. Lett.* **70**, 3995 (1993).
- ⁴⁸ J. W. Loram, K. A. Mirza, J. R. Cooper and J. L. Tallon, *J. Phys. Chem. Solids* **59** 2091 (1998).
- ⁴⁹ J. L. Cohn *et al.*, *Phys. Rev. B* **59**, 3823 (1999).
- ⁵⁰ M. Akoshima *et al.*, *Phys. Rev. B* **57**, 7491 (1998).
- ⁵¹ J. B. Mandal, A. N. Das and B. Gosh, *J. Phys. Cond. Matter* **8**, 3047 (1996).
- ⁵² C. K. Subramaniam *et al.*, *Physica (Amsterdam) C* **203** 98 (1992).
- ⁵³ C. K. Subramaniam *et al.*, *Supercond. Sci. Tech.* **7** 30 (1994).
- ⁵⁴ B. Lorenz, Z. G. Li, T. Honma and P. H. Hor, *Phys. Rev. B* **65**, 144522 (2002).
- ⁵⁵ Y. Tokunaga *et al.*, *Journal of Low Temperature Physics* **117**, 473 (1999); *Phys. Rev. B* **61**, 9707 (2000).
- ⁵⁶ T. Fujii, I. Terasaki, T. Watanabe and A. Matsuda, *Phys. Rev. B* **66**, 024507 (2002).
- ⁵⁷ Y. Cao *et al.*, *Physica (Amsterdam)* **282-287C**, 1243 (1997).
- ⁵⁸ S. Mikusu *et al.*, *Physica (Amsterdam)* **442C**, 91 (2006).
- ⁵⁹ C. K. Subramaniam, M. Paranthaman and A. B. Kaiser, *Phys. Rev. B* **51**, 1330 (1995).
- ⁶⁰ B. Wuyts, V. V. Moshchalkov and Y. Bruynseraede, *Phys. Rev. B* **53**, 9418 (1996).
- ⁶¹ M. Oda *et al.*, *Physica (Amsterdam)* **281C**, 135 (1997).
- ⁶² T. Watanabe, T. Fujii and A. Matsuda, *Phys. Rev. Lett.* **84**, 5848 (2000).
- ⁶³ K. Takenaka, K. Mizuhashi, H. Takagi and S. Uchida, *Phys. Rev. B* **50**, 6534 (1994).
- ⁶⁴ D. Bavić, J. R. Cooper, J. W. Hodby and C. Changkang, *Phys. Rev. B* **60**, 698 (1999).
- ⁶⁵ J. L. Tallon *et al.*, *Phys. Stat. Sol. (b)* **215**, 531 (1999).
- ⁶⁶ J. W. Loram, K. A. Mirza, J. R. Cooper and W. Y. Liang, *Phys. Rev. Lett.* **71**, 1740 (1993).

- ⁶⁷ V. V. Kabanov, J. Demsar, B. Podobnik and D. Mihailovic, Phys. Rev. B **59**, 1497 (1999).
- ⁶⁸ J. W. Loram, K. A. Mirza, J. R. Cooper and J. L. Tallon, Physica **282-287C**, 1405 (1997).
- ⁶⁹ J. R. Cooper and J. L. Tallon, J. Phys. I (France) **6**, 2237 (1996).
- ⁷⁰ J. W. Loram, J. L. Luo, J. R. Cooper, W. Y. Liang and J. L. Tallon, Physica (Amsterdam) **341-348C**, 831 (2000).
- ⁷¹ M. Sutherland *et al.*, Phys. Rev. B **67**, 174520 (2003).
- ⁷² D. G. Hawthorn *et al.*, Phys. Rev. B **75**, 104518 (2007).
- ⁷³ M. Chaio, R. W. Hill, C. Lupien, L. Taillefer, P. Lambert, R. Gagnon and P. Fournier, Phys. Rev. B **62**, 3554 (2000).
- ⁷⁴ J. Demsar, B. Podbnik, V. V. Kabanov, Th. Wolf and D. Mihailovic D, Phys. Rev. Lett. **82**, 4918 (1999).
- ⁷⁵ T. Takahashi, T. Sato, T. Yokoya, T. Kamiyama, Y. Naitoh, T. Mochiku, K. Yamada, Y. Endoh, K. Kadowaki, J. Phys. Chem. Solids **62**, 41 (2001).
- ⁷⁶ H. Ding, T. Yokoya, J. C. Campuzano, T. Takahashi, M. Randeria, M. R. Norman, T. Mochiku, K. Kadowaki and J. Giapintzakis, Nature **382**, 51 (1996).
- ⁷⁷ J. C. Campuzan *et al.*, Phys. Rev. Lett. **83**, 3709 (1999).
- ⁷⁸ T. Sato, H. Matsui, S. Nishina, T. Takahashi, T. Fujii, T. Watanabe and A. Matsuda, Phys. Rev. Lett. **89**, 067005 (2002).
- ⁷⁹ R. M. Dipasupil, M. Oda, N. Momono and M. Ido, J. Phys. Soc. Jpn. **71**, 1535 (2002).
- ⁸⁰ H. Ding *et al.*, Phys. Rev. Lett. **87**, 227001 (2001).
- ⁸¹ D. H. Lu *et al.*, Phys. Rev. Lett. **86**, 4370 (2001).
- ⁸² K. Tanaka *et al.*, Science **314**, 1910 (2006).
- ⁸³ D. C. Peets, New Journal of Physics **9**, 28 (2007).
- ⁸⁴ A. Damascelli, D. Hussain and Z. X. Shen, Rev. Mod. Phys. **75**, 473 (2003).
- ⁸⁵ Ch. Renner *et al.*, Phys. Rev. Lett. **80**, 149 (1998).
- ⁸⁶ N. Miyakawa *et al.*, Phys. Rev. Lett. **80**, 157 (1998).
- ⁸⁷ J. Y. T. Wei, N. -C. Yeh, D. F. Garrigus and M. Strasik, Phys. Rev. Lett. **81**, 2542 (1998).

- ⁸⁸ J. F. Zasadzinski, L. Ozyuzer, N. Miyakawa, K. E. Gray, D. G. Hinks and C. Kendziora, *Phys. Rev. Lett.* **87**, 067005 (2001).
- ⁸⁹ L. Ozyuzer, J. F. Zasadzinski and N. Miyakawa, *Int. J. Mod. Phys. B* **29-31**, 3721 (1999).
- ⁹⁰ L. Ozyuzer, J. F. Zasadzinski, C. Kendziora and K. E. Gray, *Phys. Rev. B* **61**, 3629 (2000).
- ⁹¹ K. Ishida, K. Yoshida, T. Mito, Y. Tokunaga, Y. Kitaoka, K. Asayama, Y. Nakayama, J. Shimoyama and K. Kishio, *Phys. Rev. B* **58**, 5960 (1998).
- ⁹² Y. Itoh, T. Machi, S. Adachi, A. Fukuoka, K. Tanabe and H. Yasuoka, *J. Phys. Soc. Jpn.* **67**, 312 (1998).
- ⁹³ M. Takigawa, A. P. Reyes, P. C. Hammel, J. D. Thompson, R. H. Heffner, Z. Fisk and K. C. Ott, *Phys. Rev. B* **43**, 247 (1991).
- ⁹⁴ A. Goto, H. Yasuoka and Y. Ueda, *J. Phys. Soc. Jpn.* **65**, 3043 (1996).
- ⁹⁵ B. Faqué, Y. Sidis, V. Hinkov, S. Pailhès, C. T. Lin, X. Chaud and P. Bourges, *Phys. Rev. Lett.* **96**, 197001 (2006).
- ⁹⁶ H. A. Mook, M. Yethiraj, G. Aeppli, T. E. Masson and T. Armstrong, *Phys. Rev. Lett.* **70**, 3490 (1993).
- ⁹⁷ Y. Kubo, S. Shimakawa, T. Manako and H. Igarashi, *Phys. Rev. B* **43**, 7875 (1991).
- ⁹⁸ S. Pailhès, C. Ulrich, B. Fauqué, V. Hinkov, Y. Sidis, A. Ivanov, C. T. Lin, B. Keimer and P. Bourges, *Phys. Rev. Lett.* **96**, 257001 (2006).
- ⁹⁹ G. Blumberg, M. Kang, M. V. Klein, K. Kadowaki and C. Kendziora, *Science* **278**, 1427 (1997).
- ¹⁰⁰ L. Capogna *et al.*, *Phys. Rev. B* **75**, 060502 (2007).
- ¹⁰¹ L. V. Gasparov, P. Lemmens, M. Brinkmann, N. N. Kolensnikov, G. Güntherodt, *Phys. Rev. B* **55**, 1223 (1997).
- ¹⁰² C. Kendziora and A. Rosenbergs, *Phys. Rev. B* **52**, 9867 (1995).
- ¹⁰³ S. Sugai, H. Suzuki, Y. Takayanagi, T. Hosokawa and N. Hayamizu, *Phys. Rev. B* **68**, 184504 (2003).
- ¹⁰⁴ A. A. Maksimov, I. I. Tartakovskii, M. V. Klein and B. W. Veal, *Phys. Rev. B* **49**, 15385 (1994).
- ¹⁰⁵ S. Sugai and T. Hosokawa, *Phys. Rev. Lett.* **85**, 1112 (2000).

- ¹⁰⁶ M. Kang, G. Blumberg, M. V. Klein and N. N. Kolesnikov, Phys. Rev. Lett. **77**, 4434 (1996).
- ¹⁰⁷ K. C. Hewitt and J. C. Irwin, Phys. Rev. B **66**, 054516 (2002).
- ¹⁰⁸ L. V. Gasparov, P. Lemmens, N. N. Kolesnikov, G. Gunttherodt, Phys. Rev. B **58**, 11753 (1998).
- ¹⁰⁹ M. Le. Tacon, A. Sacuto, A. Georges, G. Kotliar, Y. Gallais, D. Coloson and A. Forget, Nature Physics **2**, 537 (2006).
- ¹¹⁰ F. Venturini, M. Opel, R. Hackl, H. Berger, L. Forró and B. Revaz, J. Phys. Chem. Solids **63**, 2345 (2002).
- ¹¹¹ D. Mihailovic and V. V. Kabanov, *Superconductivity in Complex Systems*, edited by K. A. Müller and A. Bussmann-Holder (Springer, Berlin/Heidelberg, 2005), vol. 14, p. 331.
- ¹¹² T. Nakano, M. Oda, C. Manabe, N. Momono, Y. Miura and M. Ido, Phys. Rev. B **49**, 16000 (1994).
- ¹¹³ R. Yoshizaki, N. Ishikawa, H. Sawada, E. Kita and A. Tasaki, Physica (Amsterdam) **166C**, 417 (1990).
- ¹¹⁴ D. C. Johnston, Phys. Rev. Lett. **62**, 957 (1989).
- ¹¹⁵ T. Nakano, N. Momono, T. Nagata, M. Oda and M. Ido, Phys. Rev. B **58**, 5831 (1998).
- ¹¹⁶ T. Nakano, N. Momono, M. Oda and M. Ido, J. Phys. Soc. Jpn. **67**, 2622 (1998).
- ¹¹⁷ T. Sato, T. Yokoya, Y. Naitoh, T. Takahashi, K. Yamada and Y. Endoh, Phys. Rev. Lett. **83**, 2254 (1999).
- ¹¹⁸ A. Ino *et al.*, Phys. Rev. Lett. **81**, 2124 (1998).
- ¹¹⁹ A. Ino *et al.*, Phys. Rev. B **62**, 4137 (2000).
- ¹²⁰ M. Hashimoto *et al.*, Phys. Rev. B **75**, 140503 (2007).
- ¹²¹ P. Kusar, J. Demsar, D. Mihailovic and S. Sugai, Phys. Rev. B **72**, 014544 (2005).
- ¹²² Y. Itoh, T. Machi, N. Koshizuka, M. Murakami, H. Yamagata and M. Matsumura, Phys. Rev. B **69**, 184503 (2004).
- ¹²³ Y. Ando, S. Komiya, K. Segawa, S. Ono and Y. Kurita, Phys. Rev. Lett. **93**, 267001 (2004).
- ¹²⁴ T. M. Rice, Phys. World **12**, 55 (1999).

- ¹²⁵ S. Sanna *et al.*, Phys. Rev. Lett. **93**, 207001 (2004) ; S. Sanna, G. Allodi and R. De Renzi, Solid State Commun. **126**, 85 (2003) ; S. Sanna, G. Allodi, G. Concas and R. De Renzi, J. Supercond. **18**, 769 (2005).
- ¹²⁶ Ch. Niedermayer, C. Bernhard, T. Blasiud, A. Golnik, A. Moodenbaugh and J. I. Budnick, Phys. Rev. Lett. **80**, 3843 (1998) ; M. Matsuda, M. Fujita, K. Yamada, R. J. Birgeneau, Y. Endoh and G. Shirane, Phys. Rev. B **65**, 134515 (2002).
- ¹²⁷ M. Matsuda, M. Fujita, K. Yamada, R. J. Birgeneau, Y. Endoh and G. Shirane, Phys. Rev. B **65**, 134515 (2002).
- ¹²⁸ B. Watkins, H. Chashka, Y. Direktovich, A. Knizhnik, Y. Eckstein, Physica (Amsterdam) **450C**, 71 (2006).
- ¹²⁹ Risdiana, T. Adachi, N. Oki, S. Yairi, Y. Tanabe, K. Omori, Y. Koike, T. Suzuki, I. Watanabe, A. Koda and W. Higemoto, condmat-0707.3322v1; Physica C (Amsterdam) **460-462C**, 874 (2007).
- ¹³⁰ L. Krusin-Elbaum and T. Shibauchi, Int. J. Mod. Phys. B **21**, 3202 (2007).